UNIVERSITÁ DEGLI STUDI DI MILANO-BICOCCA
DIPARTIMENTO DI FISICA "G. OCCHIALINI"

CORSO DI DOTTORATO IN FISICA E ASTRONOMIA
CICLO XXVIII

Bar-formation as driver of gas inflows in isolated disc galaxies

Settore Scientifico Disciplinare FIS/05

Tesi di Dottorato di
ROSSELLA FANALI

Tutor: Dott. Massimo Dotti

Anno Accademico 2014 – 2015

Artistic representations of NGC 1300 galaxy

"Costanzia: non chi comincia,
ma quel che persevera." L. Da Vinci.

ABSTRACT

In this study I analyse the formation and evolution of a stellar bar and the gas inflow processes linked to this structure in isolated spiral galaxies. Stellar bars are a common feature in massive disc galaxies and play a fundamental role in galactic evolutionary scenarios. In particular, a bar can exert a significant torque on the gaseous disc, causing its inflow from galactic scale toward the center of the galaxy. On a theoretical ground bars are a natural consequence of the secular evolution of massive discs (Toomre, 1964; Ostriker and Peebles, 1973; Fall and Efstathiou, 1980; Mayer and Wadsley, 2004). The response of gas to a bar is generally thought to produce inner substructures such as off-axis shocks, nuclear rings and spirals in the gas distribution (Kim et al., 2012; Emsellem et al., 2015), to cause nuclear starbursts and, possibly, AGN activity once the perturbed gas reaches the central super-massive black hole.

My work is divided into two main parts: by means of high resolution numerical simulations I detail the purely dynamical effects that a forming bar exerts on the isothermal gas of an isolated disc galaxy. The galaxy is initially unstable to the formation of non-axisymmetric structures, and within ~ 1 Gyr it develops spiral arms that eventually evolve into a central

stellar bar on kpc scale. A first major episode of gas inflow occurs during the formation of the spiral arms while at later times, when the stellar bar is established, a low density region is carved between the bar co-rotational and inner Lindblad resonance radii. The development of such "dead zone" inhibits further massive gas inflows. Indeed, the gas inflow reaches its maximum during the relatively fast bar formation phase and not, as often assumed, when the bar is fully formed. I conclude that the low efficiency of long-lived, evolved bars in driving gas toward galactic nuclei is the reason why observational studies have failed to establish an indisputable link between bars and AGNs. On the other hand, the high efficiency in driving strong gas inflows of the intrinsically transient process of bar formation suggests that the importance of bars as drivers of AGN activity in disc galaxies has been overlooked so far. I finally prove that the conclusions are robust against different numerical implementations of the hydrodynamics routinely used in galaxy evolution studies. The main results of this analysis are published in A&A and MNRAS journals (Gavazzi et al., 2015; Fanali et al., 2015).

The second step of my work involves the simulations of the same galactic disc including more physical processes (namely cooling, star formation and stellar feedback). The evolution of this system is very similar to what found in the aforementioned runs. However, in this last case much of the gas inflow happens when the bar is a stable structure rather than when the bar is forming. This aspect can be explained through the possible effects of star formation and related feedback on the gas, which might delay the inflow process. These simulations also allow us to study the distribution of new stars formed during the evolution and verify that they faithfully follow the spatial distribution of stellar disc.

A further step in this work has been the study of the potential exercised on the gas to find an analytic function able to describe the bar perturbation and implementing this results in the simulation of a 2D gaseous gas.

CONTENTS

CHAPTER 1

INTRODUCTION

There are circumstantial evidences that massive black holes lurk at the centre of most massive galaxies. Their gravitational influence extends for a very small radial scale (of the order of pc). Since in a disc galaxy the gas is distributed on the whole disc plane, the central supermassive black hole cannot be the cause of the gas inflow from the outer regions of galaxies (on the order of kpc). Figure 1.1 represents two disc galaxies: in the first, NGC 4321, the gas mapped by young and blue stars is not limited to the inner part of the galaxy, but it extends in the whole radial scale of the disc. Similarly, the other two images represent M51 galaxy and, in particular, the right panel shows the CO emission from this galaxy, demonstrating that the gas trace the spiral arms trend. A possible solution for the fueling issue is the presence and the development of non-axisymmetric structures, like stellar bars.

The fraction of disc galaxies showing a well developed stellar bar in the local Universe is substantial, up to $\gtrsim 30\%$ for massive ($M_* \gtrsim 10^{9.5} M_\odot$) systems (Laurikainen et al., 2004; Nair and Abraham, 2010; Lee et al.,

Figure 1.1: Optical image of NGC 4321 from SDSS (upper left panel). Optical image of M51 from HST (lower left panel) and the corresponding CO emission (lower right panel).

2012a; Gavazzi et al., 2015). Galactic bars are considered a product of secular evolution throught interactions with the disc and the halo of a galaxy. Once a bar formed in an isolated and gas free disc, it rotates steadily with no tendency to evolve (Miller and Smith, 1979), but interaction with gas and other mass components of the galaxy can change the bar and the galaxy properties. Several studies demonstrated that models of rotationally supported stellar discs are globally unstable (Kalnajs, 1972; Jalali, 2007). In general, this instability appears like a two-arm spiral which transforms in an elongated structure in the inner part of the disc

and the spiral winds up and disappears in the outer region. The instability causes a significant rearrangement of the angular momentum in the disc and the azimuthally-averaged mass profile changes with an over density in the center (Hohl, 1971).

The effectiveness of bars in modifying the dynamics of gas has been recognized since decades (e.g. Sanders and Huntley, 1976; Roberts et al., 1979; Athanassoula, 1992). In particular, gas within the bar corotational radius (R_C, i.e. the radius at which the angular velocity in the disc plane $\Omega(R)$ equals the bar pattern precession speed Ω_b) is driven toward the centre of the galaxy because of the interaction with the bar itself. To understand the process of gas inflow due to a bar structure, in Figure 1.2 I consider a first test in which I run a disc of gas (10^6 particles) subjected to the analytical potential from Wada (2001) describing a weak perturbation, such as a bar:

$$\Phi_B(R, \phi, t) = \epsilon(R)\Phi(R)cos2(\phi - \Omega_b t), \tag{1.1}$$

where $\epsilon(R)$ is the amplitude of the perturbed potential and it is a function of radius chosen such that the perturbed force everywhere remains a small fraction of the total axisymmetric force, $\Phi(R)$ is the axisymmetric potential and Ω_b is the angular velocity of the bar. The system temporally evolves for about 15 Myr following the rows from the upper left panel to the lower right panel. In this panels I selected a single gas particle to show its path through the center of the disc during the evolution. At first, the gas particle is quite unperturbed. Then, the disc develops two spiral arms and it interacts with the bar potential and with its iterative passage. As a result, the orbit of the gas particle is modified: it is captured by the bar, it loses angular momentum and falls down through the center of the disc up to a few parsec from the center, where it lies on a ring orbit. Early theoretical studies suggested that such inflows could be responsible for

nuclear starbursts and, if the gas is able to reach the very central regions of the galaxy, AGN activity (e.g. Shlosman et al., 1989; Berentzen et al., 1998).

From the observational point of view the connection between bars and enhanced nuclear star formation has been extensively proved (e.g. Ho et al., 1997; Martinet and Friedli, 1997; Hunt and Malkan, 1999; Laurikainen et al., 2004; Jogee et al., 2005). The link between bars and AGN seems less clear: while barred galaxies host AGNs more frequently that their non-barred analogous (making bars a good candidate for the triggering of nuclear activity, e.g. Laurikainen et al., 2004; Oh et al., 2012), it is still matter of debate whether the presence of bars is one of the main drivers of AGNs (as suggested by, e.g. Knapen et al., 2000; Laine et al., 2002; Alonso et al., 2013) or not (see e.g. Ho et al., 1997; Mulchaey and Regan, 1997; Hunt and Malkan, 1999; Lee et al., 2012b; Cisternas et al., 2013)

In order to have a comprehensive understanding of the gas dynamics in barred galaxies many numerical studies have been put forward, including, for example both 2- or 3-D simulations, and different schemes for the gas hydrodynamics (smoothed particle hydrodynamics, SPH, vs grid codes). I consider particularly meaningful to divide the different efforts in three main classes:

1. **Isolated galaxies with analytical bars** (e.g. Athanassoula, 1992; Regan and Teuben, 2004; Kim et al., 2012). In this class of simulations (often restricted to a 2-D geometry) bars are represented by analytical potentials that do not evolve in time (but for their rigid body rotation). These simulations, although quite idealized, allows for extremely high resolutions and precise evolution of the gas dynamics.

2. **Fully evolving isolated galaxies** (e.g. Berentzen et al., 1998, 2007;

Villa-Vargas et al., 2010; Cole et al., 2014), where bars are modeled (as the rest of the galaxy) as evolving structures, that can change their extents, rotational patterns, etc.

3. **Cosmological simulations** (e.g. Romano-Díaz et al., 2008; Scannapieco and Athanassoula, 2012; Kraljic et al., 2012; Goz et al., 2014; Fiacconi et al., 2015; Bonoli et al., 2015). In these simulations the galaxies form from cosmological perturbations, and are free to acquire mass and angular momentum through large scale gas inflows and galaxy mergers. In this approach the initial conditions are not arbitrary, but, because of the large boxes simulated (even in zoom-in runs), the spatial and mass resolution is usually significantly coarser than in isolated simulations.

Simulations of the first kind have confirmed the analytical prediction that, in many galactic potentials, bar-driven gas inflows fail to reach the very centre of the galaxy. The gas shocks around the outermost inner Lindblad resonance (ILR) radius ($R_{\rm ILR}$) of the bar, defined by the equality $\Omega(R) - \kappa(R)/2 = \Omega_b$ where κ is the epicyclic frequency, i.e. the frequency of small radial oscillations. At $R_{\rm ILR}$ the gas shocks, forming nuclear rings that are often observed as star forming regions in barred galaxies (e.g. Kormendy, 2013, and references therein). Simulations that fully evolve the bar potential do show similar results as soon as they reach a quasi-steady state, i.e. after the bar growth transient[1]. If the gas inflows accumulates enough mass at $\sim R_{\rm ILR}$ the central region can dynamically decouple, possibly forming nested non-axisymmetric structures (e.g. nuclear bars). These structures can eventually bring the gas closer and closer to the galactic centre in a cascade-like fashion (Shlosman et al., 1989).

In this work I propose a new set of fully evolving isolated galaxies runs. I start with an unbarred galactic disc composed of stars and gas,

[1] Although promising, the coarse resolution of cosmological runs makes hard to fully resolve the nuclear region where the ILR is expected to occur.

embedded in an evolving dark matter halo. I check the dependences of the gas dynamics on different numerical implementations, varying the magnitude of an artificial viscosity (if present) and the numerical resolution (see section 4.2 for a full description of the different runs). At first, I run simulations without implementing any gas radiative cooling, star formation and stellar feedback prescriptions (usually referred to as sub-grid physics), in order to perform a clean test of the basic numerical method used, and to highlight the physical and purely dynamical effect of the forming substructures (stellar spirals and bar) onto the gas. Then, I start from the same initial system, adding physical phenomena to compare results with the first set of runs. After this analysis I study the potential which influence gas particles in the simulations and I find an analytical function to describe it.

After an outline on barred galaxies and their properties described in Chapter 2, I illustrate the codes used for the different set of simulations. Then, I report in detail the set-up of initial conditions and the features of the simulation suite in Chapter 4. I present the main findings in Chapter 5, and I finally discuss them and derive conclusions in Chapter 6.

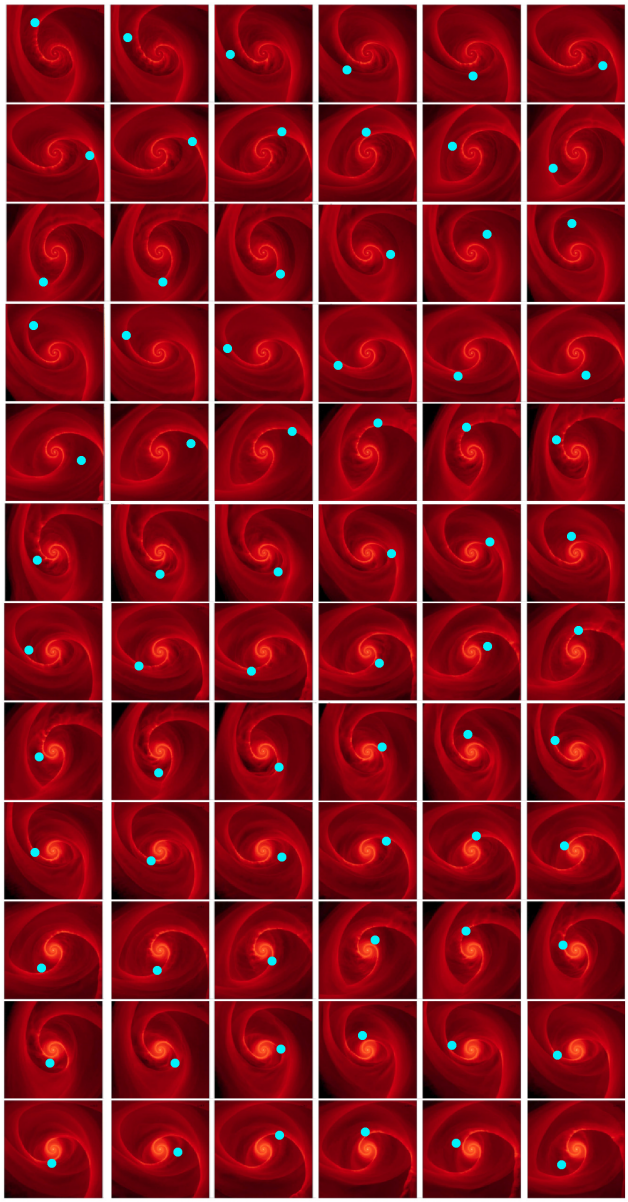

Figure 1.2: Gaseous disc simulation with the implementation of an analytic potential representing the bar. The colour gradient maps the gaseous surface density on a logarithmic scale. Each panel measures 2 bar radial scale box.

CHAPTER 2

BARRED GALAXIES

2.1 Galaxy classification

As soon as identified as entities separated from generic nebulae, galaxies have been classified depending on their morphology, in order to separate them into classes, in spite of the enormous variety of forms. The most important classification is the Hubble tuning fork, a morphological scheme for galaxies suggested by Hubble in 1926 (Hubble, 1926, 1936). He divided regular galaxies into three main classes based on their appearance:

- ellipticals E, from 0 to 7 to identify the ellipticity degree for which E0 are galaxies almost spherical, while E7 are highly flattened;
- lenticulars S0 and SB0, a disc-like structure with a central spherical bulge. They are not characterized by any spiral pattern. The SB0 galaxies show a bar that crosses the nuclear region and their subclass is defined according to the prominence of this bar; in the S0s, subclassification is dependent on the presence of gas and dust in the disc;

- spirals (S), divided into two families: barred spirals (SB) and unbarred spirals (S). Each spiral galaxies is characterized by a letter which corresponds to the arms aperture and the bulge importance (from 'a' to 'c') to mark an even increasing arms aperture and reduction of the bulge size;
- irregular, thanks to their discontinuous shape.

In Figure 2.1 is represented this classification.

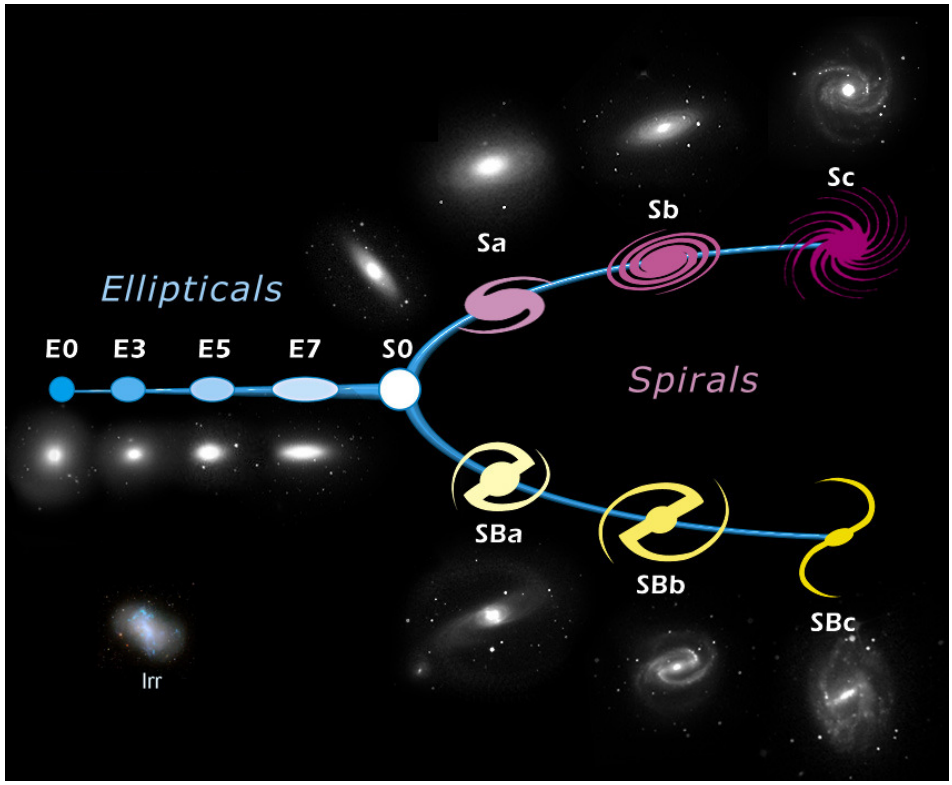

Figure 2.1: Hubble classification scheme for galaxies.

In 1959 de Vaucouleurs introduces a new classification (de Vaucouleurs, 1963) that represents an extension of the Hubble one. This scheme has an

additional degree of freedom and on the major axis are placed ellipticals, S0, spirals and irregular galaxies. The notation SA was introduced to indicate the classical spiral galaxies along with the barred ones (still identified by the Hubble's notation SB). An intermediate class (SAB) has been included for weakly barred galaxies. Even Lenticular galaxies are separated between Barred (SB0) and classical (SA0). The classification of galaxies depends also on the presence of rings-like structures (r), their absence (s) or an intermediate case (rs). The new classification includes different additional spiral classes and the relative barred counterparts: the Sd galaxies (SBd) characterized by clumpy arms and a very slight central bulge, the Sm galaxies (SBm) which are irregular galaxies apparently without any evidence of a bulge and Im galaxies, or very irregular galaxies with no clear structures such as those specified before. This complex scheme is represented in Figure 2.2.

2.2 Spiral galaxies

In the field about 60% of all galaxies are spirals, while in dense regions like galaxy clusters they are less than 10%. Spiral galaxies are composed of a *core*, characterized by a very high density of stars, a *bulge* containing the core, made of old and red stars, and a large rotating *disc* hosting spiral arms of young and blue stars, in which the star formation is very effective. Spiral galaxies produce young and blue stars mostly because of their higher fraction of cold (atomic and molecular) gas respect to other galaxies, e. g. ellipticals.
In Figure 2.3 all these component are clearly visible. This whole structure is believed to be embedded in a large and invisible *dark matter halo* which encompasses the vast majority of the galactic mass and extends well beyond the edge of the visible galaxy.

As well as stars and dark matter, spiral galaxies contain dust, atomic

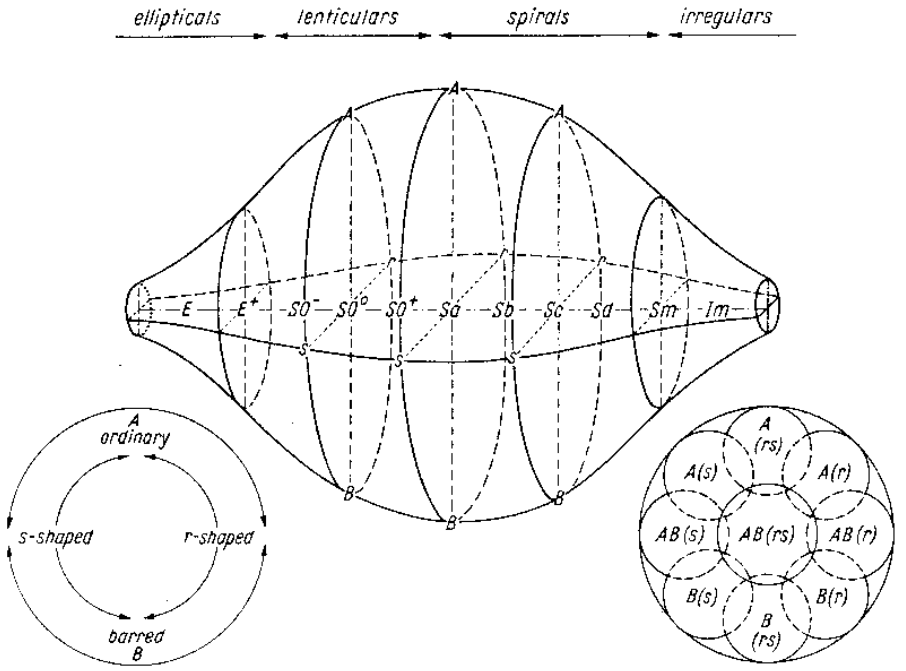

Figure 2.2: De Vaucouleurs 3D classification scheme for galaxies.

and molecular gas visible at different wavelengths. The typical radial scale for the disc in spiral galaxies is about $10 - 15$ kpc and it is extremely thin (about $< 10\%$ of radial scale). The main feature of these galaxies is the substantial role of the angular momentum which gives the object its characteristic axisymmetric shape, respect to other galaxies (e. g. ellipticals, which have a geometry of the mass distribution defined by the isotropic motion of the stars).

2.3 Bar dynamics

Up to $\geq 30\%$ for massive ($M \geq 10^{9.5} M_{\odot}$) systems in the local Universe developed a bar (Laurikainen et al., 2004; Nair and Abraham, 2010; Lee

Figure 2.3: Optical image of M83 galaxy from HST. The gas is traced by the blue and younger stars on the spiral arms and in the whole galactic disc. In the central part of the galaxy is the bulge, composed by red and older stars.

et al., 2012a; Gavazzi et al., 2015). These structures are believed to be strongly related to the secular evolution of their host spiral galaxies: the most efficient way a disc galaxy evolves is throught forming a bar via disc

instability which facilitates the redistribution of energy and angular momentum between the disc, dark matter halo and classical bulge (Debattista and Sellwood, 2000; Athanassoula, 2003; Saha et al., 2012). As the bar grows stronger, it goes through buckling instability and form boxy/peanut bulges, demonstrated in several N-body simulation studies (Combes and Sanders, 1981; Saha et al., 2012). However, the mechanisms which trigger bar formation have not been completely understood. Possible solutions can be initial perturbation caused by unequal mass mergers (where the mass ratio between the two galaxies is $q_{\rm gal} \lesssim 0.1$) or tidal interactions with companion galaxies. Several numerical simulations show that the process of bar formation is self-sustaining and the bar continues to attract ever more stars to populate the orbits which is made of. The evolution of the bar and the disc in a spiral galaxy is very correlated, because of their potential can influence each other: the evolution of bar changes the orbits of the disc particles and those can be captured by bar thanks to their interaction with the bar potential. The bar interacts with galactic material and distorts galactic orbits which in particular conditions experience dynamical resonances with the bar. For this reason, many studies show that bars can efficiently transport gas from the outer regions of galaxies to the central kiloparsec (Athanassoula, 2003; Debattista and Sellwood, 1998; Weinberg, 1985).

Morphologically, a bar is an elongated structure and in the Hubble formalism its definition depends on the angle of view (in Figure2.4 the galactic bar of NGC 1300 is shown). Because of its shape, it is difficult to observe bars in edge-on view of galaxies and their thickness is not well determined. However, since bars are so common, some limits may be obtained from the apparent thickness of the central regions of edge-on spirals. Such limits suggest that most bars are very flat, probably as flat as the discs themselves, but the bulges complicate this line of argument and it is possible that some bulges (for example, the peanut-shaped bulges)

Figure 2.4: Optical image of NGC 1300 galaxy from HST. In this figure the bar is the elongated structure which connects the two spiral arms in a kpc scale.

are the edge on view of the central and thick part of bars (Wozniak and Michel-Dansac, 2009; Yoshino and Yamauchi, 2015; Saha and Gerhard, 2013; Athanassoula, 2015).

2.3.1 Weak bar in a rotating potential

Considering a galactic disc in the frame of reference in which the potential Φ is static (i. e. corotating with the precessing bar), a star moving in a fixed sense about the center of the potential and oscillating in radius makes a loop orbit. This kind of orbit can be described as the superposition of

a circular motion and small oscillations around it. If the velocity in the co-rotating frame is $\dot{\boldsymbol{x}}$, the velocity in an inertial frame is $\dot{\boldsymbol{x}} + \boldsymbol{\Omega_b} \times \boldsymbol{x}$, where Ω_b is the angular frequency of the bar. With these assumptions, the Lagrangian is

$$L = \frac{1}{2}|\dot{\boldsymbol{x}} + \boldsymbol{\Omega_b} \times \boldsymbol{x}|^2 - \Phi(\boldsymbol{x}). \tag{2.1}$$

The momentum $\boldsymbol{p}$ can be written as

$$p = \frac{\partial L}{\partial \dot{\boldsymbol{x}}} = \dot{\boldsymbol{x}} + \boldsymbol{\Omega}_b \times \boldsymbol{x}, \tag{2.2}$$

and using the Legendre transformation the Hamiltonian in the co-rotating frame is

$$\begin{aligned} H_J &= \boldsymbol{p} \cdot \dot{\boldsymbol{x}} - L \\ &= \boldsymbol{p} \cdot [\boldsymbol{p} - \boldsymbol{\Omega}_b \times \boldsymbol{x}] - \tfrac{1}{2}p^2 + \Phi(\boldsymbol{x}) \\ &= p^2 - \dot{\boldsymbol{p}}(\boldsymbol{\Omega}_b \times \boldsymbol{x}) - \tfrac{1}{2}p^2 + \Phi(\boldsymbol{x}) \\ &= \tfrac{1}{2}p^2 + \Phi(\boldsymbol{x}) - \boldsymbol{\Omega} \cdot (\boldsymbol{x} \times \boldsymbol{p}), \end{aligned} \tag{2.3}$$

and the Hamiltonian referred to the motion in a inertial frame is

$$H = \frac{1}{2}p^2 + \Phi. \tag{2.4}$$

Then,

$$H_J = H - \boldsymbol{\Omega}_b \cdot \boldsymbol{L}. \tag{2.5}$$

Because of $\Phi(\boldsymbol{x})$ is constant in the rotating frame, H_J is not dependent on time and $\frac{dH_J}{dt} = \frac{\partial H_J}{\partial t} = 0$. This means that H_J is an integral of motion and H or $\boldsymbol{L}$ are not conserved. From eq. 2.3, the constant value H_J can

be written as

$$\begin{aligned} E_J &= \tfrac{1}{2}|\dot{\boldsymbol{x}}|^2 + \Phi - \tfrac{1}{2}|\boldsymbol{\Omega}_b \times \boldsymbol{x}|^2 \\ &= \tfrac{1}{2}|\dot{\boldsymbol{x}}|^2 + \Phi_{eff}, \end{aligned} \tag{2.6}$$

where the effective potential has been defined as

$$\begin{aligned} \Phi_{eff}(\boldsymbol{x}) &\equiv \Phi(\boldsymbol{x}) - \tfrac{1}{2}|\boldsymbol{\Omega}_b \times \boldsymbol{x}|^2 \\ &= \Phi(\boldsymbol{x}) - \tfrac{1}{2}[|\boldsymbol{\Omega}_b \times \boldsymbol{x}| \cdot |\boldsymbol{\Omega}_b \times \boldsymbol{x}|] \\ &= \Phi(\boldsymbol{x}) - \tfrac{1}{2}[|\boldsymbol{\Omega}_b \cdot \boldsymbol{\Omega}_b||\boldsymbol{x} \cdot \boldsymbol{x}| - |\boldsymbol{\Omega}_b \cdot \boldsymbol{x}_b||\boldsymbol{x} \cdot \boldsymbol{\Omega}_b|] \\ &= \Phi(\boldsymbol{x}) - \tfrac{1}{2}[|\boldsymbol{\Omega}_b|^2|\boldsymbol{x}|^2 - (\boldsymbol{\Omega}_b \cdot \boldsymbol{x})^2]. \end{aligned} \tag{2.7}$$

Equation 2.7 shows that the effective potential is composed by the sum of the gravitational potential and the repulsive centrifugal potential.

Applying Hamilton's equation to eq. 2.3, $\dot{\boldsymbol{x}}$ and $\dot{\boldsymbol{p}}$ can be calculated in the co-rotating frame as

$$\begin{aligned} \dot{\boldsymbol{p}} &= \tfrac{\partial H_J}{\partial \boldsymbol{x}} = -\nabla\Phi + \boldsymbol{p} \times \boldsymbol{\Omega}_b = -\nabla\Phi - \boldsymbol{\Omega}_b \times \boldsymbol{p}, \\ \dot{\boldsymbol{x}} &= \tfrac{\partial H_J}{\partial \boldsymbol{p}} = \boldsymbol{p} - \tfrac{\partial}{\partial \boldsymbol{p}}[\boldsymbol{p} \cdot (\boldsymbol{\Omega}_b \times \boldsymbol{x})] = \boldsymbol{p} - \boldsymbol{\Omega}_b \times \boldsymbol{x}, \end{aligned} \tag{2.8}$$

as in eq. 2.2. If we eliminate p from equations 2.8 and remembering that Ω_b is independent on time, we have

$$\begin{aligned} \ddot{\boldsymbol{x}} &= \dot{\boldsymbol{p}} - \tfrac{\partial}{\partial t}(\boldsymbol{\Omega}_b \times \boldsymbol{x}) \\ &= -\nabla\boldsymbol{\Phi} - \boldsymbol{\Omega}_b \times \boldsymbol{p} - \boldsymbol{\Omega}_b \times \dot{\boldsymbol{x}} \\ &= -\nabla\Phi - \boldsymbol{\Omega}_b \times (\dot{\boldsymbol{x}} + \boldsymbol{\Omega}_b \times \boldsymbol{x}) - \boldsymbol{\Omega}_b \times \dot{\boldsymbol{x}} \\ &= -\nabla\Phi - 2\boldsymbol{\Omega}_b \times \dot{\boldsymbol{x}} - \boldsymbol{\Omega}_b \times (\boldsymbol{\Omega}_b \times \boldsymbol{x}) \\ &= -\nabla\Phi - 2\boldsymbol{\Omega}_b \times \dot{\boldsymbol{x}} - (\boldsymbol{\Omega}_b \times \boldsymbol{x})\boldsymbol{\Omega}_b + (\boldsymbol{\Omega}_b \cdot \boldsymbol{\Omega}_b)\boldsymbol{x} \\ &= -\nabla\Phi - 2\boldsymbol{\Omega}_b \times \dot{\boldsymbol{x}} + |\boldsymbol{\Omega}_b|^2 x - \boldsymbol{\Omega}_b(\boldsymbol{\Omega}_b \cdot \boldsymbol{x}); \end{aligned} \tag{2.9}$$

in this equation we can distinguish the Coriolis force $-2\boldsymbol{\Omega}_b \times \dot{\boldsymbol{x}}$ and the centrifugal force $-\boldsymbol{\Omega}_b \times (\boldsymbol{\Omega}_b \times \boldsymbol{x})$. The gradient of the last equation in 2.7

is

$$\nabla\Phi_{eff} = \nabla\Phi - |\boldsymbol{\Omega}_b|^2\boldsymbol{x} + \boldsymbol{\Omega}_b(\boldsymbol{\Omega}_b \cdot \boldsymbol{x}), \tag{2.10}$$

and equation 2.9 becomes

$$\ddot{\boldsymbol{x}} = -\nabla\Phi_{eff} - 2\boldsymbol{\Omega}_b \times \dot{\boldsymbol{x}}. \tag{2.11}$$

Finally, to describe a perturbation, we can consider polar coordinates in the co-rotating frame (R, φ), with $\varphi = 0$ the long axis of the potential. In this configuration, $\boldsymbol{\Omega}_b$ has only a non-zero component on the z-axis, so

$$\begin{aligned} \boldsymbol{\Omega}_b \times \boldsymbol{x} &= (-\Omega_b R\sin\varphi)\hat{x}_1 + (\omega_b R\cos\varphi)\hat{x}_2 + 0\hat{x}_3 \\ &= \Omega_b R(\cos\varphi - \sin\varphi) \\ &= \Omega_b R\hat{\boldsymbol{e}}_\varphi. \end{aligned} \tag{2.12}$$

Now the Lagrangian is

$$L = \frac{1}{2}\dot{R}^2 + \frac{1}{2}[R(\dot{\varphi} + \Omega_b)]^2 - \Phi(R, \varphi), \tag{2.13}$$

and the equation 2.11 now is

$$(\ddot{R} - R\dot{\varphi}^2)\hat{\boldsymbol{e}}_R + (2\dot{R}\dot{\varphi} + R\ddot{\varphi})\hat{\boldsymbol{e}}_\varphi = 2\Omega_b R\dot{\varphi}\hat{\boldsymbol{e}}_R - 2\Omega_b\dot{R}\hat{\boldsymbol{e}}_\varphi - \nabla\Phi_{eff}. \tag{2.14}$$

where Φ_{eff} is defined in 2.7 and thanks to eq. 2.12:

$$|\boldsymbol{\Omega}_b \times \boldsymbol{x}|^2 = \Omega_b^2 R^2, \tag{2.15}$$

and

$$\begin{aligned} &(\ddot{R} - R\dot{\varphi}^2)\hat{\boldsymbol{e}}_R + (2\dot{R}\dot{\varphi} + R\ddot{\varphi})\hat{\boldsymbol{e}}_\varphi \\ &= 2\Omega_b R\dot{\varphi}\hat{\boldsymbol{e}}_R - 2\Omega_b\dot{R}\hat{\boldsymbol{e}}_\varphi - \nabla\Phi + \tfrac{1}{2}\nabla(\Omega_b^2 R^2). \end{aligned} \tag{2.16}$$

Now we derive the equation of motion in the polar frame, consider each

component separately. For the $\hat{\boldsymbol{e}}_R$ component we have:

$$\begin{aligned} \ddot{R} - R\dot{\varphi}^2 &= 2\Omega_b R\dot{\varphi} - \tfrac{\partial\Phi}{\partial R} + \tfrac{1}{2}\tfrac{\partial}{\partial R}(\Omega_b^2 R^2) \\ &= 2\Omega_b R\dot{\varphi} + \Omega_b^2 R - \tfrac{\partial\Phi}{\partial R} \\ \ddot{R} &= R(\dot{\varphi}^2 + 2\Omega_b\dot{\varphi} + \Omega_b^2) - \tfrac{\partial\Phi}{\partial R}, \end{aligned} \tag{2.17}$$

and for the $\hat{\boldsymbol{e}}_\varphi$ component we have:

$$\begin{aligned} &2\dot{R}\dot{\varphi} + R\ddot{\varphi} = -2\Omega_b\dot{R} - \tfrac{1}{R}\tfrac{\partial\Phi}{\partial\varphi} + \tfrac{1}{2R}\tfrac{\partial}{\partial\varphi}(\Omega_b^2 R^2) \\ &2R\dot{R}(\dot{\varphi} + \Omega_b) + R^2\ddot{\varphi} = -\tfrac{\partial\Phi}{\partial\varphi}. \end{aligned} \tag{2.18}$$

Then, the equations of motion in a 2D rotating potential in polar coordinates are:

$$\begin{aligned} &\ddot{R} = R(\dot{\varphi} + \Omega_b)^2 - \tfrac{\partial\Phi}{\partial R} \\ &\tfrac{\mathrm{d}}{\mathrm{dt}}[R^2(\dot{\varphi} + \Omega_b)] = -\tfrac{\partial\Phi}{\partial\varphi}. \end{aligned} \tag{2.19}$$

2.3.2 Epicyclic frequency and resonances

We can now consider a disc galaxy with a weak bar. Assuming that the bar rotates at some steady pattern speed Ω_b, in the frame that rotates with its potential, the equation of motion in polar coordinates (R, φ) are derived in eq. 2.19. The total potential of the galaxy is composed by the axisymmetric disc contribution $\Phi_0(R)$ and the non-axisymmetric bar contribution $\Phi_1(R, \varphi)$, such as

$$\Phi(R, \varphi) = \Phi_0(R) + \Phi_1(R, \varphi), \tag{2.20}$$

where $|\Phi_0/\Phi_1| \ll 1$, since the bar is a weak perturbation. We divide R and φ into zeroth- and first-order parts (assuming quasi-circular orbits)

$$R(t) = R_0 + R_1(t); \qquad \varphi(t) = \varphi_0(t) + \varphi_1(t); \tag{2.21}$$

with the assumption that the term R_0 is constant with time. Substituting these expressions into eq. 2.19, it yields

$$\begin{aligned} \ddot{R_1} =& (R_0 + R_1)(\dot{\varphi_0} + \dot{\varphi_1} + \Omega_b)^2 - \left(\frac{\partial \Phi_0}{\partial R}\right)_{R_0} \\ & - \left(\frac{\partial^2 \Phi_0}{\partial R^2}\right)_{R_0} R_1 - \left(\frac{\partial \Phi_1}{\partial R}\right)_{R_0} - \left(\frac{\partial^2 \Phi_1}{\partial R^2}\right)_{R_0} R_1, \end{aligned} \tag{2.22}$$

and to

$$\frac{d}{dt}[(R_0 + R_1)^2(\dot{\varphi_0} + \dot{\varphi_1} + \Omega_b)] = -\left(\frac{\partial \Phi_1}{\partial \varphi}\right)_{\varphi_0(R_0)} - \left(\frac{\partial^2 \Phi_1}{\partial \varphi^2}\right)_{\varphi_0(R_0)} \varphi_1, \tag{2.23}$$

remembering that Φ_0 does not depend on the coordinate φ and that the expansion is about the radius R_0. If the sum of the zeroth-order terms is set to zero, it follows that

$$R_0(\dot{\varphi_0} + \Omega_b)^2 = \left(\frac{d\Phi_0}{dR}\right)_{R_0}, \tag{2.24}$$

and to

$$\frac{d}{dt}[R_0^2 \dot{\varphi_0} + \Omega_b] = 0 \quad \dot{\varphi_0} = constant. \tag{2.25}$$

It corresponds to the equation for centrifugal equilibrium at R_0. Defining $\Omega_0 \equiv \Omega(R_0)$ where the circular frequency at R in the potential Φ_0 as

$$\Omega(R) \equiv \pm\sqrt{\frac{1}{R}\frac{d\Phi_0}{dR}}, \tag{2.26}$$

the eq. 2.25 becomes

$$\dot{\varphi_0} = \Omega_0 - \Omega_b, \tag{2.27}$$

where prograde orbits occur for $\Omega_0 > 0$ and retrograde ones for $\Omega_0 < 0$, assuming $\Omega_b > 0$. The origin of time is set as

$$\varphi_0(t) = (\Omega_0 - \Omega_b)t. \tag{2.28}$$

So, from the equations of motions in eq. 2.19 we obtain

$$\begin{aligned} &\ddot{R_1} + \left(\frac{d^2\Phi_0}{dR^2} - \Omega^2\right)_{R_0} R_1 - 2R_0\Omega_0\dot{\varphi_1} = -\left(\frac{\partial\Phi_1}{\partial R}\right)\Bigg|_{R_0}, \\ &\ddot{\varphi_1} + 2\Omega_0\frac{\dot{R_1}}{R_0} = -\frac{1}{R_0^2}\left(\frac{\partial\Phi_1}{\partial\varphi}\right)\Bigg|_{R_0}. \end{aligned} \tag{2.29}$$

Now we can choose a specific form of Φ_1

$$\Phi_1(R,\varphi) = \Phi_b(R)\cos(\mathrm{m}\varphi), \tag{2.30}$$

with m a positive integer number and $m = 2$ means have a barred potential. Assuming that $\varphi_1 \ll 1$, $\varphi(t)$ is close to $(\Omega_0 - \Omega_b)t$. If we replace φ

by φ_0 in the expression for $\frac{\partial \Phi_1}{\partial R}$ and $\frac{\partial \Phi_1}{\partial \varphi}$ we obtain:

$$\begin{aligned} \ddot{R}_1 + \left(\tfrac{d^2\Phi_0}{dR^2} - \Omega^2\right)_{R_0} R_1 - 2R_0\Omega_0\dot{\varphi}_1 = \\ -\left(\tfrac{\partial \Phi_b}{\partial R}\right)_{R_0} \cos[m(\Omega_0 - \Omega_b)t], \\ \ddot{\varphi}_1 + 2\Omega_0 \tfrac{\dot{R}_1}{R_0} = -\tfrac{m\Phi_b(R_0)}{R_0^2} \sin[m(\Omega_0 - \Omega_b)t]. \end{aligned} \tag{2.31}$$

Integrating the second equation we have:

$$\dot{\varphi}_1 = -2\Omega_0 \frac{R_1}{R_0} - \frac{\Phi_b(R_0)}{R_0^2(\Omega_0 - \Omega_b)} \cos[m(\Omega_0 - \Omega_b)t] + \text{constant}. \tag{2.32}$$

If we eliminate $\dot{\varphi}_1$ from the first equation of 2.31, the result is:

$$\begin{aligned} \ddot{R}_1 + \kappa_0^2 R_1 = -\left[\frac{d\Phi_b}{dR} + \frac{2\Omega\Phi_b}{R(\Omega - \Omega_b)}\right]_{R_0} \\ \cos[m(\Omega_0 - \Omega_b)t] + \text{constant}, \end{aligned} \tag{2.33}$$

where

$$\kappa_0^2 \equiv \left(\frac{d^2\Phi_0}{dR^2} + 3\Omega^2\right)_{R_0} = \left(R\frac{d\Omega^2}{dR} + 4\Omega^2\right)_{R_0} \tag{2.34}$$

is the **epicyclic frequency**. Equation 2.33 is the equation of motion of a harmonic oscillator of natural frequency κ_0 that is driven at frequency

$m(\Omega_0 - \Omega_b)$. The general solution to this equation is

$$R_1(t) = C_1 \cos(\kappa_0 t + \alpha) - \left[\frac{d\Phi_b}{dR} + \frac{2\Omega\Phi_b}{R(\Omega - \Omega_b)}\right]_{R_0} \frac{\cos[m(\Omega_0 - \Omega_b)t]}{\Delta}, \quad (2.35)$$

with C_1 and α arbitrary constants, and

$$\Delta \equiv \kappa_0^2 - m^2(\Omega_0 - \Omega_b)^2. \quad (2.36)$$

Using the eq. 2.28 to eliminate t from the eq. 2.35 we find

$$R_1(\varphi_0) = C_1 \cos\left(\frac{\kappa_0 \varphi_0}{\Omega_0 - \Omega_\mathrm{b}} + \alpha\right) + \mathrm{C_2 cos(m}\varphi_0), \quad (2.37)$$

with

$$C2 \equiv -\frac{1}{\Delta}\left[\frac{d\Phi_b}{dR} + \frac{2\Omega\Phi_b}{R(\Omega - \Omega_b)}\right]_{R_0}. \quad (2.38)$$

If $C_1 = 0$, $R_1(\varphi_0)$ is periodic in φ_0 with period $2\pi/m$ and the orbit corresponds to a closed loop orbit.

When the epicyclic frequency is synchronous with the relative motion of the bar in the absence of gravitational forcing by the wave, a phenomenon called *resonance* occurs. In this formalism this happens when the right side of eq. 2.38 for R_1 becomes singular, such as for some values of R_0 and we can distinguish three different group of resonance:

- *Corotation resonance* (**CR**). When

$$\Omega_0 = \Omega_b, \quad (2.39)$$

$\dot{\varphi_0} = 0$ and it corresponds to the radius where the stars of the disc orbit at the same angular velocity of the bar.

- *Inner Lindblad Resonance* (**ILR**). When

$$m(\Omega_0 - \Omega_b) = +\kappa_0, \tag{2.40}$$

the frequency of stars exceed the frequency of the bar at the resonant frequency κ_0. When stars iteratively are in the same position respect to the bar, they interact increasingly strong with it near this resonance.

- *Outer Lindblad Resonance* (**OLR**). When

$$m(\Omega_0 - \Omega_b) = -\kappa_0, \tag{2.41}$$

the frequency of stars is slower then the frequency of the bar at the resonant frequency k_0.

The ILR and OLR are connected. A circular orbit has two natural frequencies: if the star is displaced it oscillates at the epicycle frequency k_0. If the star is displaced but it is still in a circular orbit, it continues on a circular orbit displaced from the original one. Then, its natural azimuthal frequency is zero. The two different resonances originate between the forcing frequency seen by star $m(\Omega_0 - \Omega_b)$ and the two frequencies κ_0 ad 0.

2.3.3 Particle orbits

In a spiral galaxy, stars and gas travel in nearly circular orbits in the equatorial plane. Their radial coordinate R wobble periodically because of the perturbations due to the gravitational effects of other objects and

to initial, random velocity components of the molecular cloud from which they formed. If these orbits are closed, they are elliptical and they are called *epicycles*. The particles move inward and outward in the disk with a *epicyclic frequency* and the oscillations are due to the conservation of angular momentum, operating through the Coriolis force: if a particle is going slower than the average motion at that radius it falls inward because of its centrifugal force cannot balance the gravitational force of the inner galaxy. Once the particle falls inward, the Coriolis acceleration is directed in the opposite sense and the particle increases its circular speed. This causes an increase in the centrifugal force on the gravitational one and the particle moves outward. The result of this process is a regular inward and outward, forward and backward oscillation in its orbit. In Figure2.5 the epicyclic oscillation of a particle in the disc is represented.

In the vicinity of the bar, stellar orbits are very different from those in the disc plane. Figure 2.6 shows the orientation of star orbits inside a bar. Inside the ILR, orbits are perpendicular to the bar and they are called x_2. Outside the ILR, orbits are parallel to the bar and they are called x_1 orbits. Their behaviour can be explained by eq. 2.37, where for $m = 2$ the closed loop orbit is aligned with the bar whenever $C_2 > 0$, and is aligned perpendicular to the bar when $C_2 < 0$. When R_0 passes through a Lindblad resonance, the sign of C_2 and the orientation of the closed loop orbits change.

The bar potential also influences the path of gas in the disc, modifying its orbits. Through this mechanism, several kind of peculiar shapes are created, often in correspondence of the resonance phenomena. For example, the end of spiral arms is assumed to be near the OLR because it is a resonance radius according to rotation curve and pattern speed fits to several design galaxies. An other feature are rings, close to the ILR: the gas moves to the center of the galaxy influenced by the bar and stops its falling, lying in a ring orbit. In Figure 2.7 these main features are shown

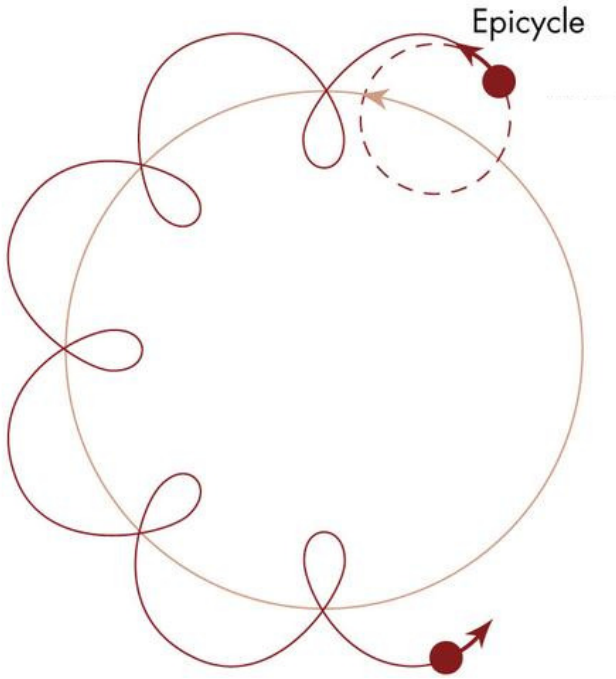

Figure 2.5: Representation of an epicyclic oscillation. The arrows represent the relative directions of rotation of the disc and epicycle.

for a real galaxy.

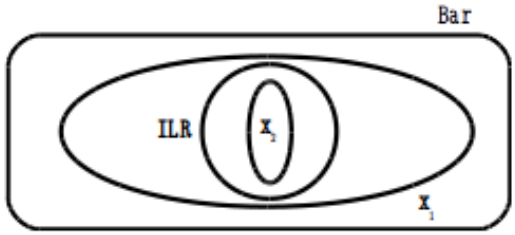

Figure 2.6: Orientation of star orbits inside a bar. Inside the ILR, orbits are perpendicular to the long axis of bar (x_2 orbits) and outside ILR are parallel (x_1 orbits).

Figure 2.7: Optical image of NGC 3351 galaxy from HST. This galactic disc presents evident spiral arms populated by young stars. In the inner part of the disc when spiral arms stop, a circular structure is visible, corresponding to the ILR ring.

CHAPTER 3

NUMERICAL METHODS

In astrophysics, numerical simulations are the most powerful tool to study very complex systems and non-trivial issues, comparing results with observations or predict their evolution and behaviour.

In this work I used two codes: GADGET2 (Springel, 2005) and GIZMO (Hopkins, 2014) and in the next sections I describe their main features.

3.1 GADGET2

GADGET2 (GAlaxies with Dark matter and Gas intEracT, Springel (2005)) is a public Smoothed Particle Hydrodynamics (SPH) tree-code direcly derived from the simulation code GADGET-1 (Springel et al., 2001). Differently from traditional Eulerian methods, which discretizes space and represents fluid variables on a mesh, GADGET2 presents a Lagrangian methods that discretizes mass using, for example, a set of fluid particles to model the flow. Lagrangian methods like SPH are particularly well-suited to follow the gravitational growth of structure, and to automatically increase the resolution in the central regions of galactic haloes, which are

the regions of primary interest in cosmology.

Gravitational forces

GADGET2 evaluates gravitational forces using the tree method, according to which particles are in a hierarchy of groups.

The force of which each particle is affected by distant groups is approximated by its lower moments of a multiple expansion. Then, the computational cost for the acceleration is $O(NlogN)$ (Appel, 1985). The code considers only the monopole moment to develop calculations (Springel, 2005). The gravitational acceleration of particles is computed as follows: the computational domain is hierarchically subdivided into a series of cubes (Figure 3.1). Each cube contains eight sub-cubes with half the side-length of the previous. These cubes are the nodes of the tree structure. Each node contains a single particle or is progenitor for other nodes. In GADGET2 each node carries the acceleration exerted by the single particle contained within the total monopole moment of all the particles located inside the cube.

Once the division has been carried out, the force exerted by the node onto each particle is evaluated using the monopole term of the gravitational potential produced by the particles inside the corresponding node.

The system of particles is considered a collisionless system. For this reason the code defines a sphere around each particle in which the mass is smoothed. The so called gravitational softening (ϵ) is the radius of this sphere and the smoothing is defined as

$$\rho(r) = m_i W(r/\epsilon), \tag{3.1}$$

where the smoothing kernel used is a spline of the form Monaghan and

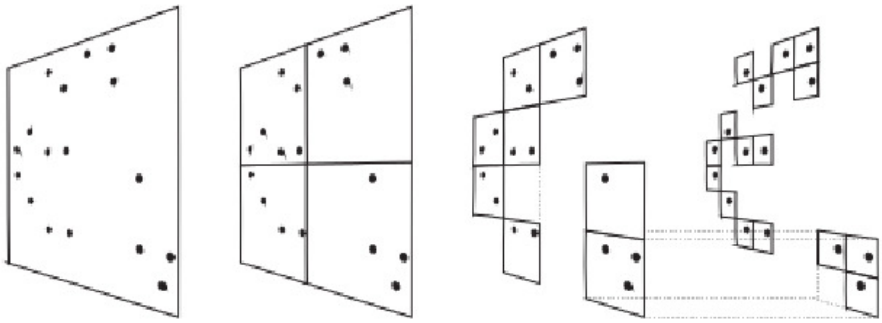

Figure 3.1: Representation of the Barnes & Hut oct-tree in the two-dimensional case (from Springel et al. 2001).

Lattanzio (1985)

$$W(u) = \frac{8}{\pi\epsilon^3}\begin{cases} 1-6u^2+6u^3, & 0 \le u \le \frac{1}{2}, \\ 2(1-u)^3, & \frac{1}{2} < u \le 1, \\ 0, & u > 1; \end{cases} \tag{3.2}$$

where $u = r/\epsilon$. In the general softened gravity case the function becomes

$$g(r) = -\frac{1}{\epsilon}W_2(u), \tag{3.3}$$

where

$$W_2(u) = \begin{cases} \frac{16}{3}u^2 - \frac{48}{5}u^4 + \frac{32}{5}u^5 - \frac{14}{5}, & 0 \le u < \frac{1}{2}, \\ \frac{1}{15}u^{-1} + \frac{32}{3}u^2 - 16u^3 + \frac{48}{5}u^4 - \frac{32}{15}u^5 - \frac{16}{5}, & \frac{1}{2} \le u < 1, \\ -u^{-1}, & u \ge 1. \end{cases} \tag{3.4}$$

Then, the gravitational force acting on each particle is evaluated by travelling the tree and summing the different contribution of force derived

from each node considered.

Hydrodynamics

The code estimates the hydrodynamic force and the variation of internal energy determining new smoothing lengths h_i for gas particles and for each of them the neighbouring particles inside their respective smoothing radii are found. By varying the smoothing length h_i of each particle, the number of neighbours is kept exactly equal. Once smoothing lengths are computed, the hydrodynamical properties of the gas (i.e. pressure, internal energy and density) and the hydrodynamical forces can be evaluated.

In GADGET2, the density computation of a gaseous particle is evaluated as:

$$\rho_i = \sum_{j=1}^{N} m_j W(|\mathbf{r_{ij}}|, h_i), \tag{3.5}$$

where $\mathbf{r_{ij}} \equiv \mathbf{r_i} - \mathbf{r_j}$ is the distance between i and j particles and $W(r, h)$ has the same form of the smoothing kernel of equation (3.2). The smoothing length h_i of each particle is the radius of a sphere containing gaseous mass, i.e. the smoothing length and the estimated densities respond to this equation:

$$\frac{4\pi}{3} h_i^3 \rho_i = N_{SPH} \bar{m}, \tag{3.6}$$

where N_{SPH} is the typical number of smoothing neighbours, and $\bar{m}$ is an average particle mass.

The particle pressure is given by $P_i = A_i \rho_i^{\gamma}$, where A_i is the entropy of each particle, which remains constant in absence of shocks and external sources of heat, and γ is the polytropic index of gas. However, flows of ideal gas can develop discontinuities and entropy can be generated by microphysics. These shocks are captured thanks to the implementation of

an artificial viscosity, that results in a viscous force:

$$\left.\frac{\mathrm{d}v_i}{\mathrm{d}t}\right|_{\mathrm{visc}} = -\sum_{j=1}^{N} m_j \prod_{ij} \nabla_i \bar{W}_{ij}, \tag{3.7}$$

where $\bar{W}_{ij}$ is the arithmetic average of the two kernels $W_{ij}(h_i)$ and $W_{ij}(h_j)$, while $\prod_{ij} \geq 0$ is the Gingold and Monaghan (1977) form of the artificial viscosity of the form

$$\prod_{ij} = (-\alpha c_{ij}\mu_{ij} + \beta\mu_{ij}^2)/\rho_{ij} \qquad \text{if} \qquad \boldsymbol{v}_{ij}\cdot\boldsymbol{r}_{ij} < 0 \tag{3.8}$$

and zero otherwise with

$$\mu_{ij} = \frac{h_{ij}\boldsymbol{v}_{ij}\cdot\boldsymbol{r}_{ij}}{|\boldsymbol{r}_{ij}|^2} \tag{3.9}$$

h_{ij} and ρ_{ij} are arithmetic means of the corresponding quantities for i and j particles, while c_{ij} is the mean sound speed. The strength of the viscosity is regulated by the parameters α and β, with typical values $\alpha \simeq 0.8$ and $\beta = 2\alpha$ in the runs. In the equation of motion, the viscosity acts like an excess pressure assigned to particles not explicitly depending on the smoothing length, but on w/c where w is the relative velocity projected onto the separation vector.

The internal energy evolves as:

$$\frac{\mathrm{d}u_i}{\mathrm{d}t} = \frac{1}{2}\sum_j m_j \left(\frac{P_i}{\rho_i^2} + \frac{P_j}{\rho_j^2} + \tilde{\prod_{ij}}\right)(\boldsymbol{v_i}-\boldsymbol{v_j})\left[\frac{1}{2}\nabla_i W(r_{ij};h_i)+\frac{1}{2}\nabla_i W(r_{ij};h_i)\right] \tag{3.10}$$

and is set at the beginning of the simulation for each gas particle.

3.2 GIZMO

GIZMO is a meshfree code that captures advantages from both SPH and grid codes: it preserves the Lagrangian structure of SPH codes, but at the same time solved directly the Euler equations among different regions of the computational domain without requiring the implementation of any artificial viscosity. I used it in its finite-mass variant, in which there is not mass flux among the regions belonging to different particles, keeping the mass of each gas particle fixed. This code includes star formation, radiative cooling and many additional physics and the evaluation of gravitational forces derives directly from GADGET2, explained in Section 3.1. GIZMO also allow to consider cosmological scenarios but in this work is not required.

Hydrodynamics

The Euler equations are a set of conservation laws of mass, momentum and energy which form a system of partial differential equations in a frame moving at a velocity $\boldsymbol{v}_{frame}$ of the form:

$$\frac{\partial \boldsymbol{U}}{\partial t} + \nabla \cdot (\boldsymbol{F} - \boldsymbol{v}_{frame} \otimes \boldsymbol{U}) = \boldsymbol{S}, \tag{3.11}$$

where $\boldsymbol{S}$ is a source function for $\boldsymbol{U}$, the "state vector" of conserved variables,

$$\boldsymbol{U} = \begin{pmatrix} \rho \\ \rho \boldsymbol{v} \\ \rho e \end{pmatrix} = \begin{pmatrix} \rho \\ \rho \boldsymbol{v} \\ \rho u + \frac{1}{2}\rho |\boldsymbol{v}^2| \end{pmatrix} = \begin{pmatrix} \rho \\ \rho v_x \\ \rho v_y \\ \rho v_z \\ \rho u + \frac{1}{2}\rho |\boldsymbol{v}^2| \end{pmatrix}, \tag{3.12}$$

where ρ is mass density, e is the total specific energy, u is the specific internal energy and the tensor $\boldsymbol{F}$ is the flux of conserved variables

$$\boldsymbol{F} = \begin{pmatrix} \rho\boldsymbol{v} \\ \rho\boldsymbol{v} \otimes \boldsymbol{v} + P\boldsymbol{I} \\ (\rho e + P)\boldsymbol{v} \end{pmatrix}, \tag{3.13}$$

with P the pressure and $\boldsymbol{I}$ the identity tensor. Multiplying equation 3.11 by an arbitrary test function ϕ integrating over the domain Ω and evaluating the integration by parts of the $\phi\nabla \cdot \boldsymbol{F}$ term we obtain:

$$0 = \int_{\Omega} (\dot{U}\phi - \boldsymbol{F} \cdot \nabla\phi - \boldsymbol{S}\phi) d\Omega + \int_{\partial\Omega} (\boldsymbol{F}\phi) \cdot \hat{n}_{\partial\Omega} d\partial\Omega, \tag{3.14}$$

where $\hat{n}_{\delta\Omega}$ is the normal vector to the surface $\delta\Omega$. If fluxes and/or ϕ vanish at infinity, integrating the term $\dot{U}\phi$ by parts results:

$$0 = \int_{\Omega} (\boldsymbol{U}(\boldsymbol{x}, t)\dot{\phi} + \boldsymbol{F}(\boldsymbol{U}, \boldsymbol{x}, t) \cdot \nabla\phi + \boldsymbol{S}(\boldsymbol{x}, t)\phi) d^{\nu}\boldsymbol{x} dt. \tag{3.15}$$

The domain volume onto a set of particles i with coordinates $\boldsymbol{x}_i$ can be discretized considering a differential volume $d^{\nu}\boldsymbol{x}$ at arbitrary coordinates $\boldsymbol{x}$ and divide this differential volume fractionally among the nearest particles through the use of a weighting function W, i. e. associate a fraction $\psi_i(\boldsymbol{x})$ of the volume $d^{\nu}\boldsymbol{x}$ with particle i according to a function $W((\boldsymbol{x} - x_i), h(\boldsymbol{x}))$:

$$\psi_i(\boldsymbol{X}) \equiv \frac{1}{\omega(\boldsymbol{x})} W((\boldsymbol{x} - x_i), h(\boldsymbol{x})) \tag{3.16}$$

$$\omega(\boldsymbol{X}) \equiv \sum_j W((\boldsymbol{x} - x_i), h(\boldsymbol{x})) \tag{3.17}$$

where $h(\boldsymbol{x})$ is the "kernel size" that enters W. The weighting function determines how the volume at any point $\boldsymbol{x}$ should be partitioned among

the volumes associated with the tracer points i (Gaburov and Nitadori, 2011). An example is shown in Figure 3.2 where this method (left panel) is compared with the volume partitions used in moving-mesh (central panel) and SPH methods (right panel).

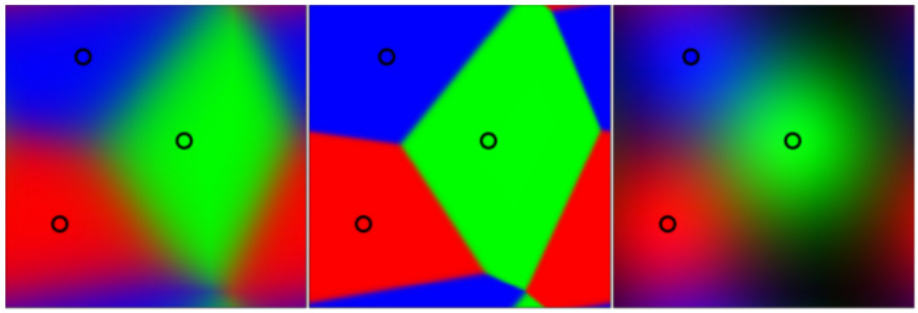

Figure 3.2: Representation of differences between the method used in this code (left panel), the mesh methods (central panel) and the SPH method (right panel).

Including this volume partition into equation 3.15, Taylor-expanding all terms to second order accuracy in the smoothing length $h(\boldsymbol{x})$ and applying this to the integral of an arbitrary function we obtain:

$$\begin{aligned}\int f(\boldsymbol{x})d^{\nu}\boldsymbol{x} = \sum_i \int f\boldsymbol{x}\psi_i(\boldsymbol{x})d^{\nu}\boldsymbol{x} &= \sum_i f_i(\boldsymbol{x}_i)\int \psi d^{\nu}\boldsymbol{x} + O(h_i(\boldsymbol{x}_i)^2) \\ &\equiv \sum_i f_i V_i + O(h_i^2),\end{aligned} \tag{3.18}$$

where $V_i = \int \psi_i(\boldsymbol{x})d^{\nu}\boldsymbol{x}$ is the effective volume of particle i, such as the integral of its volume partition over all of space and f is an arbitrary

function. Then, for equation 3.15 we obtain:

$$0 = \int dt \sum_i (V_i \boldsymbol{U}_i \dot{\phi}_i) + V_i \boldsymbol{F}_i \cdot (\nabla \phi)_{\boldsymbol{x}=\boldsymbol{x}_i} + V_i \boldsymbol{S}_i \phi_i) \tag{3.19}$$

where $\boldsymbol{F}_i \cdot (\nabla \phi)_{\boldsymbol{x}=\boldsymbol{x}_i}$ refers to the product of the matrix $\boldsymbol{F}$ with the gradient of ϕ evaluated at $\boldsymbol{x}_i$. Considering the second-order discrete gradient estimator described in many previous numerical studies (Gaburov and Nitadori, 2011), inserting it in equation 3.15 and integrating by parts again, we have

$$0 = \int dt \sum_i \phi_i \bigg(- \frac{d}{dt}(V_i \boldsymbol{U}_i) - \sum_j [V_i \boldsymbol{F}_i^\alpha \tilde{\psi}_j^\alpha(\boldsymbol{x}_i) - V_j \boldsymbol{F}_j^\alpha \tilde{\psi}_i^\alpha(\boldsymbol{x}_j)] + V_i \boldsymbol{S}_i \bigg). \tag{3.20}$$

The expression inside the parenthesis must vanish because eq. 3.20 must hold for any arbitrary test function ϕ. So

$$\frac{d}{dt}(V_i \boldsymbol{U}_i) + \sum_j [V_i \boldsymbol{F}_i^\alpha \tilde{\psi}_j^\alpha(\boldsymbol{x}_i) - V_j \boldsymbol{F}_j^\alpha \tilde{\psi}_i^\alpha(\boldsymbol{x}_j)] = V_i \boldsymbol{S}_i. \tag{3.21}$$

Taking the flux functions $\boldsymbol{F}$ at the particle location and time of i or j would require some ad-hoc artificial dissipation terms (for example viscosity) to be stable, then the fluxes can be replaced with the solution of an appropriate time-centered Riemann problem between the particles i and j, which includes the dissipation terms. So, defining the flux as $\tilde{\boldsymbol{F}}_{ij}$ that replaces $\boldsymbol{F}_i$, $\boldsymbol{F}_j$ and the vector $\boldsymbol{A}_{ij} = |A|_{ij} \hat{A}_{ij}$ where $\boldsymbol{A}_{ij}^\alpha \equiv V_i \tilde{\psi}_j^\alpha(\boldsymbol{x}_i) - V_j \tilde{\psi}_i^\alpha(\boldsymbol{x}_j)$, the equation becomes

$$\frac{d}{dt}(V_i \boldsymbol{U}_i) + \sum_j \tilde{\boldsymbol{F}}_{ij} \cdot \boldsymbol{A}_{ij} = V_i \boldsymbol{S}_i. \tag{3.22}$$

The term $V_i \boldsymbol{U}_i$ is the particle-volume integrated value of the conserved quantity to be carried with particle i, its time rate of change is given by

the sum of the fluxes $\tilde{\boldsymbol{F}}_{ij}$ into/out of an effective face area $\boldsymbol{A}_{ij}$, plus the total integral of source terms over the volume associate to the particle $V_i \boldsymbol{S}_i$.

3.3 GADGET-2 vs GIZMO

For the simulations presented in this work I use two different codes: GADGET-2 and GIZMO. GADGET-2 is very useful to study astrophysical systems using the SPH method for the hydrodynamics of gas with a Lagrangian approach. Anyway, the Eulerian equations are solved in differential form and they vanish when the fluid has discontinuities (e.g. shocks). To correctly solve these discontinuities, the integral form should be used. For this reason it is necessary to implement an artificial viscosity term with the effect of dissipating relative motions of the fluid into heat, converting kinetic energy of gas particles in internal energy.

On the other hand, GIZMO solves explicitly the Eulerian equations, without requiring any artificial viscosity term. Furthermore, in this code we can implement physical processes such as cooling, star formation and stellar feedback. This kind of code allow us to study the effect of these phenomena on gas and supposedly approach to the simulation of real galaxies.

CHAPTER 4

SIMULATIONS

In this chapter I describe the features of the runs. I start with an unbarred isolated galactic disc composed of stars and gas, embedded in an evolving dark matter halo. I check the dependences of the gas dynamics on different numerical implementations, varying the magnitude of the artificial viscosity (if present) and the numerical resolution. First, I run simulations without implementing any gas radiative cooling, star formation and stellar feedback prescriptions (usually referred to as sub-grid physics), in order to perform a clean test of the basic numerical method used, and to highlight the physical and purely dynamical effect of the forming substructures (stellar spirals and bar) onto the gas. Then, I run simulations implementing physical processes and I compare the corresponding results with the first set of simulations.

4.1 Initial conditions

I simulate the isolated disc galaxy model Lmd2c12 described by Mayer and Wadsley (2004), in order to reproduce an initially bulgeless, bar-unstable

disc galaxy. The galaxy model is made of three different components: a dark matter halo, a stellar and a gaseous disc.

The dark matter halo follows the Navarro et al. (NFW 1996, 1997) density profile:

$$\rho_{\rm h}(r) = \frac{\rho_{\rm crit}\ \delta_{\rm c}}{(r/r_{\rm s})(1+r/r_{\rm s})^2}, \tag{4.1}$$

where $r_{\rm s}$ is the scale radius of the halo, $\rho_{\rm crit}$ is the critical density of the Universe today[1], and:

$$\delta_{\rm c} = \frac{200}{3}\frac{c^3}{\log(1+c) - c/(1+c)}, \tag{4.2}$$

depends only on the concentration parameter $c \equiv r_{200}/r_{\rm s}$. r_{200} is the radius that encompasses an average density $\langle\rho\rangle = 200\ \rho_{\rm crit}$ and defines the outer radius of the dark matter halo. The mass of the halo is therefore $M_{200} = 200\ \rho_{\rm crit}\ (4\pi/3)\ r_{200}^3$. I adopt $c = 12$ and a scale velocity $v_{200} = \sqrt{GM_{200}/r_{200}} = 75$ km s^{-1}, which corresponds[2] to $M_{200} = 1.4 \times 10^{11}$ M$_\odot$, $r_{200} = 100$ kpc and $r_{\rm s} = 9.2$ kpc. Both stellar and gaseous discs are modeled as a radial exponential disc with a vertical structure modelled as an isothermal sheet (Hernquist, 1993):

$$\rho_\star(R,z) = \frac{M_\star}{4\pi R_\star^2 z_\star}\exp(-R/R_\star)\ \cosh^{-2}\left(\frac{z}{z_\star}\right), \tag{4.3}$$

where $R_\star = 3$ kpc is the radial scale length and $z_\star = 0.3$ kpc is the vertical scale height. The stellar disc has a total stellar mass $M_\star = 1.4 \times 10^{10}$ M$_\odot$ and extends up to $10R_\star$. The gas component has a mass $M_{\rm gas} = 0.05M_\star = 7 \times 10^8$ M$_\odot$ and its density profile is characterized by the same parameters $R_\star$ and $z_\star$. The gas has a uniform temperature $T_0 = 10000$ K and I

[1] I assume $H_0 = 71$ km s^{-1} Mpc^{-1}, compatible with the *Wilkinson Microwave Anisotropy Probe* 7/9 years cosmology (Komatsu et al., 2011; Hinshaw et al., 2013)

[2] These numbers are slightly different from those reported by Mayer and Wadsley (2004) because of the different cosmology assumed. However, this does not affect the evolution of the galaxy model.

assume that it is composed of a mixture of ionized hydrogen and helium with a mean molecular weight $\mu \simeq 0.59$. All the parameters are chosen in agreement with the galaxy-halo scalings predicted by the Λ-CDM model (e.g. Mo et al., 1998).

I build the initial conditions using the code GINCO[3]. GINCO initializes quasi-equilibrium galaxy models following Hernquist (1993) and Springel et al. (2005). The polar/spherical coordinates of the particles that belong to each component are randomly sampled using the density profiles as probability distribution functions. Then, polar/spherical angles are randomly drawn and they are used to determine the Cartesian coordinates of the particle positions.

The velocities are sampled from local Gaussian approximations of the true distribution function (Hernquist, 1993). The position-dependent parameters of the Gaussians are computed solving the steady-state Jeans equations with some closure assumptions on the velocity dispersion tensor (see e.g. Binney and Tremaine, 2008). For spherical components (i. e. the dark matter halo, since the simulated system is bulgeless), I assume that the velocity dispersion tensor is isotropic (i.e. of the form $\sigma^2(r)\,\mathbb{I}$, where $\mathbb{I}$ is the identity matrix), with the 1D velocity dispersion given by:

$$\sigma^2(r) = \frac{1}{\rho(r)} \int_r^{+\infty} \rho(x) \frac{\mathrm{d}\Phi_{\mathrm{tot}}}{\mathrm{d}r}(x)\ \mathrm{d}x, \tag{4.4}$$

where $\rho(r)$ is the density profile of the considered component and Φ_{tot} is the total gravitational potential. The spherical components have no net rotation. The potential of the halo is an analytic function; instead, the potential of the disc is computed as a first-order vertical perturbation of the potential of a razor-thin exponential disc, namely $\Phi_{\mathrm{d}}(R, z) \simeq \Phi_0(R) +$

[3]GINCO (Galaxy INitial COnditions, http://www.ics.uzh.ch/∼fiacconi/software.html) has been written by Davide Fiacconi.

$\Phi_1(R,z)$. The razor-thin disc has the potential:

$$\Phi_0(R) = -\frac{GM_\star}{R_\star}\ y\ \left[I_0(y)K_1(y) - I_1(y)K_0(y)\right], \tag{4.5}$$

where $y = R/(2R_\star)$ and I_i and K_i are modified Bessel functions; the first-order vertical perturbation is (e.g. Binney and Tremaine, 2008):

$$\begin{aligned}\Phi_1(R,z) &\equiv 4\pi G \int_0^z \mathrm{d}z' \int_0^{z'} \mathrm{d}z'' \rho_\star(R,z'') \\ &= 4\pi G\ \rho(R,0)\ z_\star^2\ \log\left[\cosh\left(\frac{z}{z_\star}\right)\right].\end{aligned} \tag{4.6}$$

I use this strategy to maintain all the evaluations of the potentials and of their derivatives analytic; this makes the code faster and reduces the required memory. Once I compute $\sigma^2(r)$, I can sample the magnitude of the velocity of each particle in a spherical component from a Maxwellian distribution with variance $\sigma^2(r)$. Finally, I randomly draw the spherical angles (θ,ϕ) as above to ensure isotropy and I assign the Cartesian components of the velocity.

Both the stellar and the gaseous disc velocity structure is characterized by a velocity dispersion tensor of the form $\mathrm{diag}(\sigma_r^2,\sigma_\phi^2,\sigma_z^2)$. The vertical velocity dispersion is (Hernquist, 1993; Springel et al., 2005):

$$\begin{aligned}\sigma_z^2(R,z) &= \frac{1}{\rho_\star(R,z)} \int_z^{+\infty} \rho_\star(R,z') \frac{\partial \Phi_{\mathrm{tot}}}{\partial z}(R,z')\ \mathrm{d}z' \\ &\approx \frac{GM_\star z_\star}{2R_\star^2} \exp\left(-\frac{R}{R_\star}\right),\end{aligned} \tag{4.7}$$

where the last approximation holds when the disc is geometrically thin and the vertical gradient of the potential around $z \simeq 0$ is dominated by the disc. The radial component is chosen to be $\sigma_r^2 \propto \sigma_z^2$, with the normalization enforcing a minimum value of the Toomre parameter $\mathcal{Q} \simeq$

1.1 at $r \simeq 2.5R_\star$ (Mayer and Wadsley, 2004). The whole profile of $\mathcal{Q}$ for the initial conditions is shown in Figure 4.1. The azimuthal component is set using the epicyclic approximation, $\sigma_\phi^2 = \sigma_r^2\ \kappa^2/(4\Omega^2)$. Unlike the dark matter halo, the disc has a net rotation, i.e. an average azimuthal velocity $\langle v_\phi \rangle$ given by (Hernquist, 1993; Springel et al., 2005):

$$\langle v_\phi \rangle^2 = V_\mathrm{c}^2 + \sigma_r^2 \left(1 - \frac{\kappa^2}{4\Omega^2} - \frac{2R}{R_\star}\right), \tag{4.8}$$

where V_c is the circular velocity in Φ_tot. Finally, I sample the (v_r, v_ϕ, v_z) components of the velocity of each disc (both star and gas) particles from Gaussian distributions with mean $(0, \langle v_\phi \rangle, 0)$ and standard deviations $(\sigma_r, \sigma_\phi, \sigma_z)$, respectively, and I finally transform then into the Cartesian components.

I checked the stability of initial conditions studying the evolution of the stellar surface density profile as a function of time (upper panel of Figure 4.2) during the first Gyr, i.e. before the development of strong non-axisymmetric perturbation (see below). After a short transient phase due to the non-exact equilibrium of the initial conditions (highlighted be the yellow line in figure) the system re-adjust on a profile similar to the initial one, with the surface density at $t = 1$ Gyr (red line) differing by 20% at most with respect to the initial conditions (within the disc scalelength). Similar conclusions about the stability of the stellar disk can be drawn from the evolution of its Lagrangian radii (lower panel of Figure 4.2).

4.2 Simulation suite

I run a suite of numerical simulations of the reference model described in the previous Section in order to explore the effects of resolution, numerical implementation, parametrization of the artificial viscosity and feedbacks associated to different physical processes (when present). In Table 4.1 I

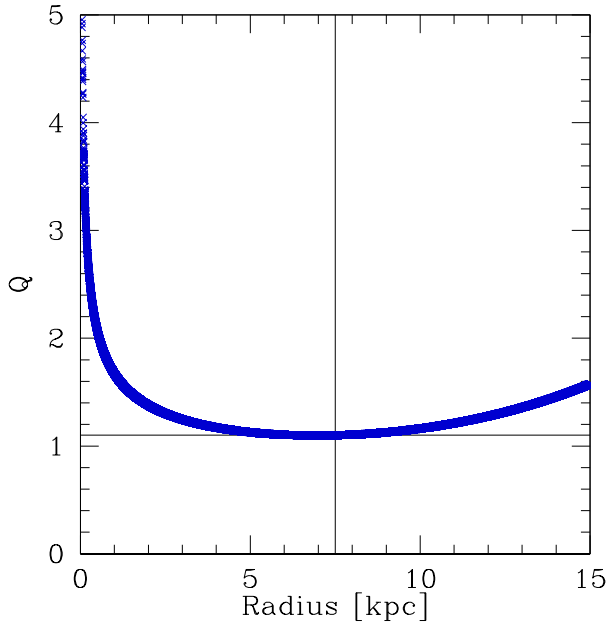

Figure 4.1: Radial profile for the Toomre parameter of the initial stellar disc.

summarize the sample of 3D runs presented in this work. I build two realizations of the initial conditions at two resolutions:

1. low resolution (LR): the halo is sampled with 10^6 particles with mass $m_{\rm h} = 1.4 \times 10^5$ M$_\odot$, while the stellar and gaseous discs are sample with 9.5×10^5 and 5×10^4 particles, respectively, with mass $m_\star = m_{\rm gas} \simeq 1.5 \times 10^4$ M$_\odot$. The gravitational softenings (setting the spatial/force resolution of the gravitational interaction) for dark matter and baryonic particles (equal for stars and gas particles) are 65 pc and 20 pc, respectively;

2. high resolution (HR): the halo is sampled with 8×10^6 particles with mass $m_{\rm h} = 1.6 \times 10^4$ M$_\odot$, while the stellar and gaseous discs are

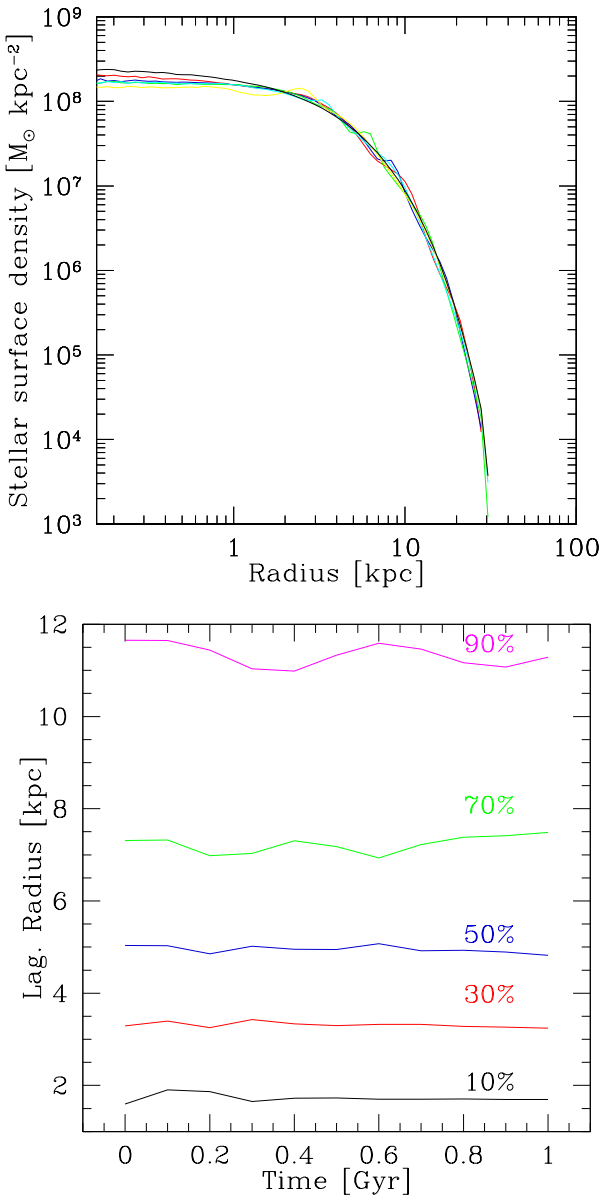

Figure 4.2: Upper panel: surface density profile of the stellar component in the first Gyr. Black, yellow, cyan, green, blue and red curves correspond to t =0, 0.2, 0.4, 0.6, 0.8 and 1 Gyr, respectively. Lower panel: Lagrangian radius at different stellar mass fraction in the first Gyr. Black, red, blue, green and magenta lines represent 10%, 30%, 50%, 70%, 90% of stellar mass, respectively.

sample with 7.6×10^6 and 4×10^5 particles, respectively, with mass $m_\star = m_{\rm gas} \simeq 1.7 \times 10^3$ $\mathrm{M}_\odot$. The gravitational softenings for dark matter and baryonic particles are 30 pc and 7 pc, respectively.

At first, I report low and high resolution simulations for a bar-unstable disc mainly using the code GADGET2. I ensure that the particles in the disc (star and gas) have all the same mass, preventing any spurious relaxation/mass segregation. All the simulations assume an isothermal equation of state to simply model an effective atomic radiative cooling keeping the ISM in the disc plane at an almost constant temperature $\lesssim 10^4$ K. Metal line and molecular cooling would reduce the gas temperature further, allowing for dense clumps to form and to trigger star-formation. Feedback from stars would then re-heat the gas, resulting in the formation of a multi-phase medium (e.g. Wada, 2001; Wada and Norman, 2001). Because of the lack of cooling and star-formation physics, I keep an high temperature to prevent the sudden fragmentation of the gaseous disc. I test the robustness of the results against two different implementations of the hydrodynamics. Most of the simulations are performed with the Tree/Smoothed Particle Hydrodynamics (SPH) code GADGET2 (Springel, 2005), which uses an oct-tree structure to speed up the gravity calculations (Barnes and Hut, 1986) and deal the hydrodynamics with the density-entropy SPH approach proposed by Springel and Hernquist (2002). The SPH formalism requires the introduction of an artificial viscosity in order to capture shocks correctly (e.g. Monaghan, 1992; Balsara, 1995; Monaghan, 1997). Therefore, I explore the effect of different choices of the value of the artificial viscosity parameter α[4], comparing the results with a simulation using the code GIZMO that solves the evolution of the gas on an unstructured grid and does not require any explicit artificial viscosity term.

[4]The β parameter in the Monaghan-Balsara formulation is equal to 2 α in all our runs.

Finally, I analyze analogous low and high resolution simulations performed with the code GIZMO (Hopkins, 2014). The public version of the code only provides basic gravity and hydrodynamics. In the simulations I included cooling, star formation and stellar feedback implemented in Lupi et al. 2015 (in prep.): radiative cooling is computed by means of the GRACKLE[5] chemistry and cooling library, which provides both equilibrium and non-equilibrium chemistry for primordial species and metals (Bryan et al., 2014; Kim et al., 2014). Gas is eligible for star formation when three conditions are fulfilled: the density exceeds $\rho = 10$ cm^{-3}, the temperature drops below $T = 2 \times 10^4$ K and the gas particles belong to a converging flow. I set the star formation efficiency to 0.05. Gas is converted into stars according to the Schmidt law (Kennicutt, 1998), following the stochastic prescription described in Stinson et al. (2006).

Each stellar particle represents a population described by the Chabrier Initial Mass Function (IMF) (Chabrier, 2003). Stars with masses in the range 8-40 M$_\odot$explode as type II SNae after a typical lifetime obtained from Hurley et al. (2000) for stars with different masses and metallicities. In order to model non thermal processes energising the SNa associated blastwave, the code implements a cooling shut-off recipe like the one described in Stinson et al. (2006), which temporarily inhibits radiative cooling for gas particles within the SNa maximum extension radius R_E, as defined in Chevalier (1974). In the simulations I consider a shut-off time of 5 Myr.

[5]http://grackle.readthedocs.org

Table 4.1: Summary of simulations characteristics. Columns: (1) name of the simulation, (2-3) resolution, (4) code used, (5) artificial viscosity α.

Name	Barion particle softening (pc)	DM particle softening (pc)	Code	α
LR	20	65	GADGET2	0.8
LRV16	20	65	GADGET2	1.6
LRV04	20	65	GADGET2	0.4
LRGiz	20	65	GIZMO	-
HR	7	30	GADGET2	0.8
LRPh	20	65	GIZMO	-
HRPh	7	30	GIZMO	-

CHAPTER 5

RESULTS

I run a suite of hydrodynamical simulations of an isolated disc galaxy model in order to explore the effect of resolution and physical processes. In this chapter I present the main results. In section 5.1.1 and 5.1.2 I propose low and high resolution simulations for a bar-unstable disc mainly using the code GADGET2. In section 5.2.1 and 5.2.2 I show low and high resolution simulations implementing cooling, star formation and stellar feedback using the code GIZMO. Finally, I pay particular attention to the central region of the galaxy and the boxy-peanut like structure formed in these systems.

5.1 Isothermal runs

5.1.1 Low resolution simulations (LR)

Figure 5.1 shows the distribution of stars and gas observed in the LR run at three different times, $t = 1$, 4 and 7 Gyr on the left, central and right panels respectively. The stellar surface density is shown in the upper and

middle panels (edge-on and face-on views, respectively), while the face-on view of the gas surface density is shown in the lower panels.

During the first 2 Gyr the bar-unstable system evolves from an axisymmetric configuration to a barred disc, passing through the formation of transient multi-arm spirals. In particular, a three arm spiral structure is observable in the stellar density distribution at $t = 1$ Gyr in the left-middle panel of Figure 5.1. From 2 Gyr on, the disc shows a clear bar structure (with a diameter size of about 8 kpc) in its central region. From the bar-formation time ($t \approx 2$ Gyr) on, the bar tends to slow-down, as shown in the upper panel of Figure 5.2. At $t \lesssim 3$ Gyr the bar makes almost 2.8 full precessions per Gyr, while the frequency decreases down to $\lesssim 2.3$ precessions per Gyr at $t \approx 7$ Gyr. The bar slow-down, already extensively discussed in literature (e.g. Sellwood, 1981; Combes and Sanders, 1981; Halle et al., 2015), results in a $R_{\rm ILR}$ growing in time, from ~ 1 kpc up to ~ 1.4 kpc at the end of the run, as observable in the lower panel of Figure 5.2. The bar forms thin, and buckles in its centre as the time goes by, as observable in the edge-on view of the stellar disc at $t = 4$ and 7 Gyr. At the end of the simulation a boxy-peanut bulge like structure is observable within the central few kpc of the disc.

The dynamics of the subdominant gas component is dominated by the underlying stellar dynamics. During the first 2 Gyr the gas distribution resembles the stellar one, with clear spiral arms observable (almost co-spatial with the stellar ones, see the example in the left lower panel of Figure 5.1 at t =1 Gyr). After the formation of the stellar bar, the gas within the bar corotational radius ($R_{\rm C} \approx$ 4-5 kpc depending on the age of the bar, as will be discussed below) is driven toward the galaxy centre, and forms a dense knot of gas clearly observable in the central and right panels in the bottom row of Figure 5.1. The torquing effect of the spiral arms before and the stellar bar afterwards sweeps the almost totality of the gas between $R_{\rm C}$ and the central dense knot. A small amount of low dense gas

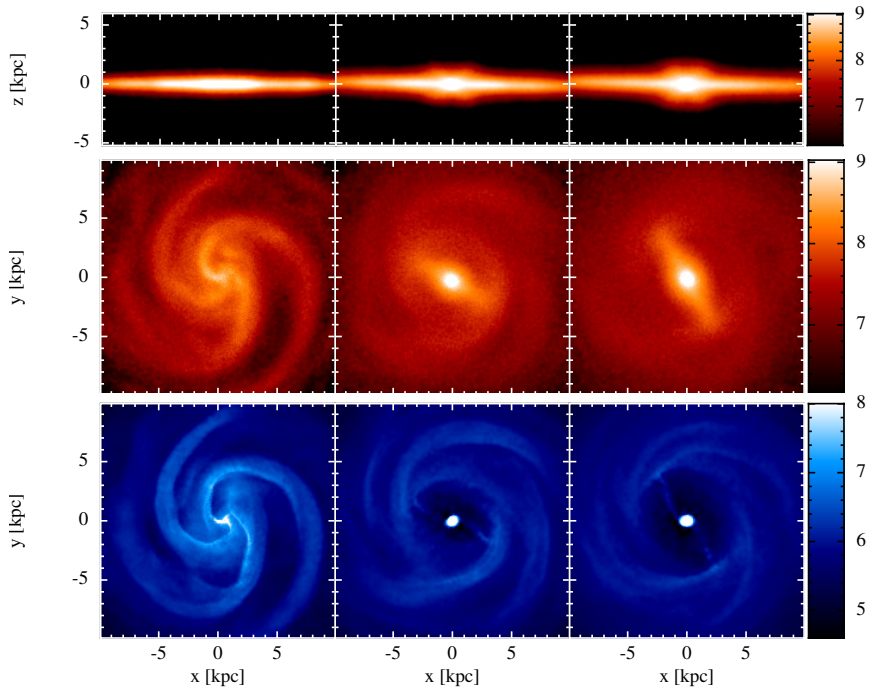

Figure 5.1: *LR simulation.* Upper (middle) panels: edge-on (face-on) views of the stellar disc at t =1, 4 and 7 Gyr (left, central and right panel, respectively). The colour gradient maps the stellar surface density (in units of $M_\odot$ kpc^{-2}) on a logarithmic scale. Bottom panels, same as the middle panel for the gas surface density.

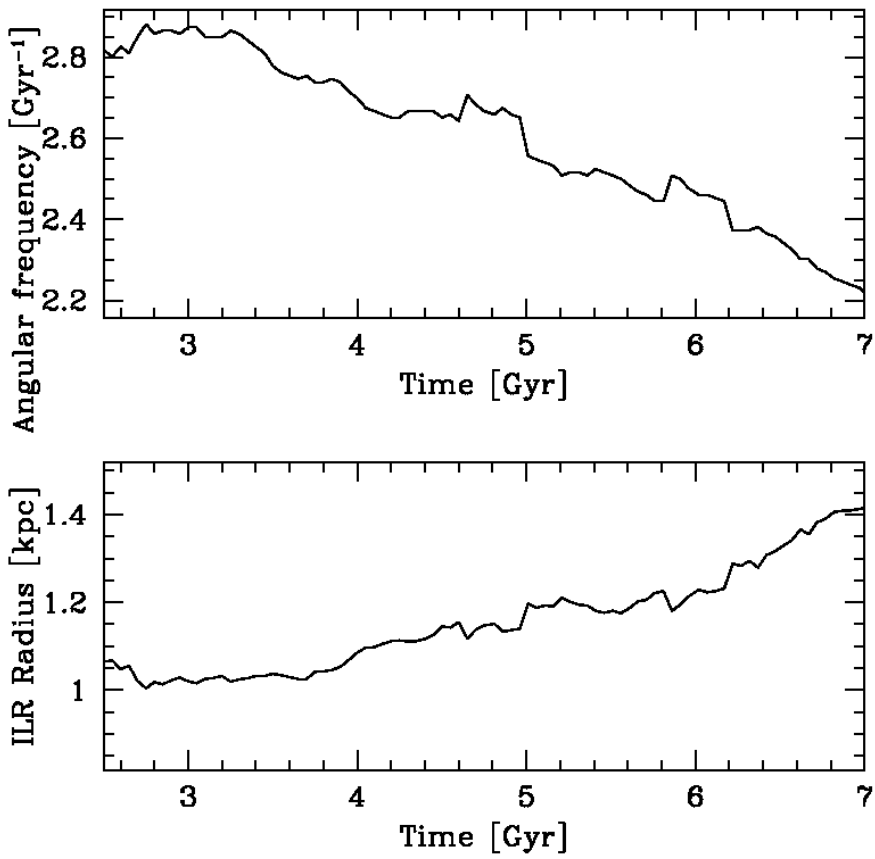

Figure 5.2: *LR simulation.* Angular frequency of the bar (upper panel) and radius corresponding to the inner Lindblad resonance from t=2.5 to t=7 Gyr (lower panel).

is still observable in this "dead region", in particular in the form of two inflowing streams connecting the outer galactic disc with the central dense knot, often observed in simulations as well as in real galaxies (e.g. Regan et al., 1999).

The upper panel of Figure 5.3 quantifies the effect that the bar formation process has onto the gas. The surface density of the gas in the "dead zone" decreases by up to ~ 1.5 orders of magnitude at $t \gtrsim 3$ Gyr (blue, yellow and red lines) with respect to the initial conditions (black line). The shaded areas in figure trace the evolution of $R_{\rm C}$ (green) and its outermost inner Lindblad resonance radius ($R_{\rm ILR}$ pink), from when a clear bar structure is observable and its angular frequency is measurable ($t \approx 2$ Gyr) to the end of the simulation. The gas within $R_{\rm C}$ is dragged toward scales of the order of $R_{\rm ILR}$, fuelling the formation of the central knot of gas on sub-kpc scales (in agreement with a wealth of previous studies, e.g. Sanders and Huntley, 1976; Shlosman et al., 1989; Athanassoula, 1992; Berentzen et al., 1998; Regan and Teuben, 2004; Kim et al., 2012; Cole et al., 2014), where the surface density increases by up to almost 2 orders of magnitude.

A clear although less obvious result of the LR run consists in the efficiency of the "dead zone" formation. Most of the inflow from $R < R_{\rm C}$ to $R \lesssim R_{\rm ILR}$ happens during the first 2 Gyr, as observable comparing the cyan (t =1 Gyr), green (t =2 Gyr) and blue (t =3 Gyr) lines with the initial conditions and the end result of the simulation in the upper panel of Figure 5.3. The fully formed bar does indeed play a role in further decreasing the gas surface density on the "dead zone", and most importantly, in preventing new gas to refill the central regions by pushing the gas immediately outside the CR toward the outer Lindblad resonance radius ($R_{\rm OLR}$).[1] However, it is instead the formation of the bar which is

[1] Although harder to be noticed in a log-log plot, the gas surface density decreases in the $R_{\rm C} < R < R_{\rm OLR}$ region, and the material accumulates just outside $R_{\rm OLR}$.

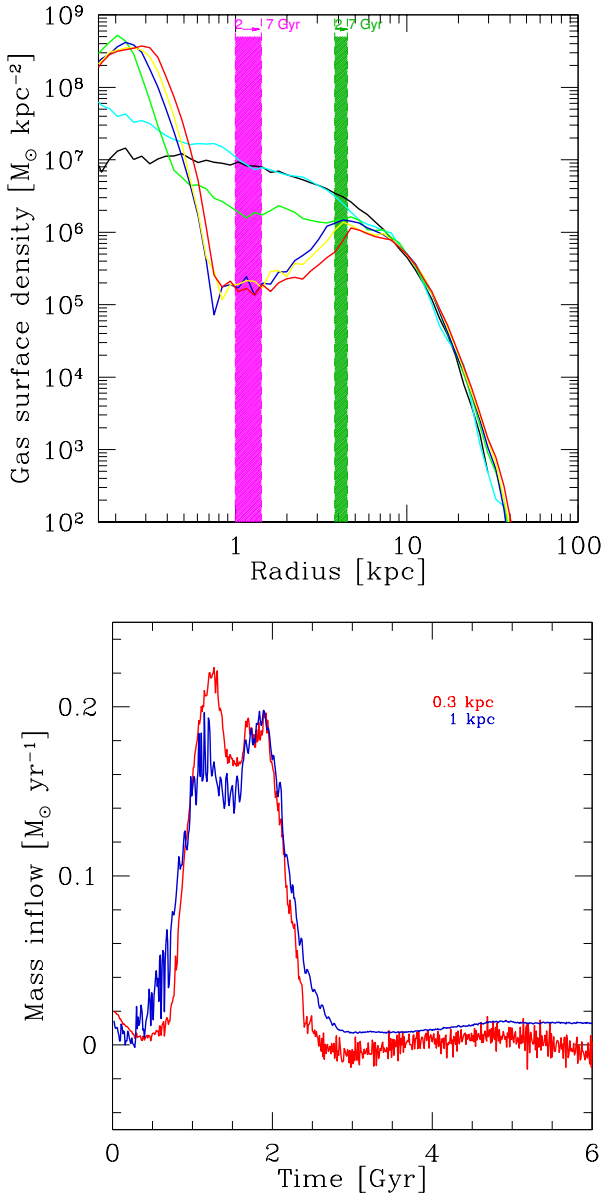

Figure 5.3: *LR simulation.* Upper panel: surface density profile of the gaseous component. Solid black, cyan, green, blue, yellow and red curves correspond to t =0, 1, 2, 3, 5 and 7 Gyr, respectively. The shaded magenta and green areas mark the region span by $R_{\rm ILR}$ and $R_{\rm C}$, respectively. Lower panel: gaseous mass inflow as a function of time. Red and blue lines represent the accretion rate computed at 0.3 and 1 kpc from the center, respectively.

efficient in driving substantial gas inflow. The fundamental importance of the torques acting on the gas during the build-up of the bar, before this has been fully developed, is highlighted in the lower panel of Figure 5.3, in which I show the gas accretion rate $\dot{M}$ as a function of time. In particular, the red and blue lines refer to $\dot{M}$ through surfaces at 0.3 and 1 kpc from the centre, respectively. At both scales $\dot{M}$ shows a first prominent peak at $t \approx 1$ Gyr, well before the formation of any significant bar-like structure. A second peak of similar magnitude is observable at $t \approx 2$ Gyr, just after the bar has formed, while the central fuelling drops immediately afterwards. Although this simple simulation does not include any star formation prescription, such omission has little impact on the evolution of the gas from R_C down to the nuclear knot, since the majority of the inflow happens on a few (up to ≈ 10 close to $R_{\rm ILR}$) orbital timescales. The time evolution of the accretion flows through the two surfaces is quite similar at all times.

Viscosity test

As recently reviewed by Sellwood (2014), the gas angular momentum transport in SPH simulations could be at least partially affected by the artificial viscosity used. Differently from grid based codes, in which a numerical viscosity is intrinsically related with the discretization of the space domain, in SPH codes the numerical viscosity is explicitly taken into account through a viscosity parameter α. The shear and bulk viscosity in SPH simulations scale linearly with α (e.g. Murray, 1996; Lodato and Price, 2010).

In this section I test the effect of the artificial viscosity through the comparison of run LR with three different simulations. Two of these, LRV04 and LRV16, are exact copies of the LR run, but for the value of the α parameter, that is half and double of the $\alpha = 0.8$ value used in LR. The third simulation (LRGiz) has been run using the GIZMO code

(Hopkins, 2014), that solves the evolution of the gas on an unstructured grid and does not require any explicit artificial viscosity term.

The results of the test are shown in Figure 5.4 and Figure 5.5. Figure 5.4 shows the comparison between the surface density profiles of the four runs (LR in red, LRV16 in green, LRV04 in blue and LRGiz in cyan) at four different times, t =1 Gyr (upper left panel), 3 Gyr (upper right panel), 5 Gyr (lower left panel) and 7 Gyr (lower right panel). Similarly, Figure 5.5 shows the face-on projection of the gas surface density map for the four runs at $t = 1$ Gyr, to allow for a comparison of the non-axisymmetric structures forming. The comparison between the three SPH runs shows that the exact value of the viscosity parameter α plays a little role in the gas dynamics. The removal of gas from the forming "dead zone" and the formation of a dense central gas knot are completely dominated by the gravitational torques due to the formation of non-axisymmetric structures. The LRGiz run shows some very minor differences too.

5.1.2 High resolution simulation (HR)

I run an increased resolution version of the LR simulation (HR). Because of the higher spatial resolution and of the isothermal equation of state implemented, the gas in the HR run forms extremely dense and compact clouds in the galaxy nucleus, slowing down the simulation enormously after the first episode of major gas inflow. For this reason I have run the HR simulation only up to $t \approx 3$ Gyr, and I limit our analysis to the response of the gas to the initial spiral and bar formation.

Figure 5.6 shows the face-on views of the stellar (left panels) and gaseous (right panels) surface density. Similarly to the low resolution simulation, during the first Gyr, the system develops stellar spiral arms (upper left panel) which evolve in a stable bar like structure (lower left panel) at about $t = 2.5$ Gyr. The gas follows a similar dynamics as observed in the lower resolution run, following the stellar spiral arms during

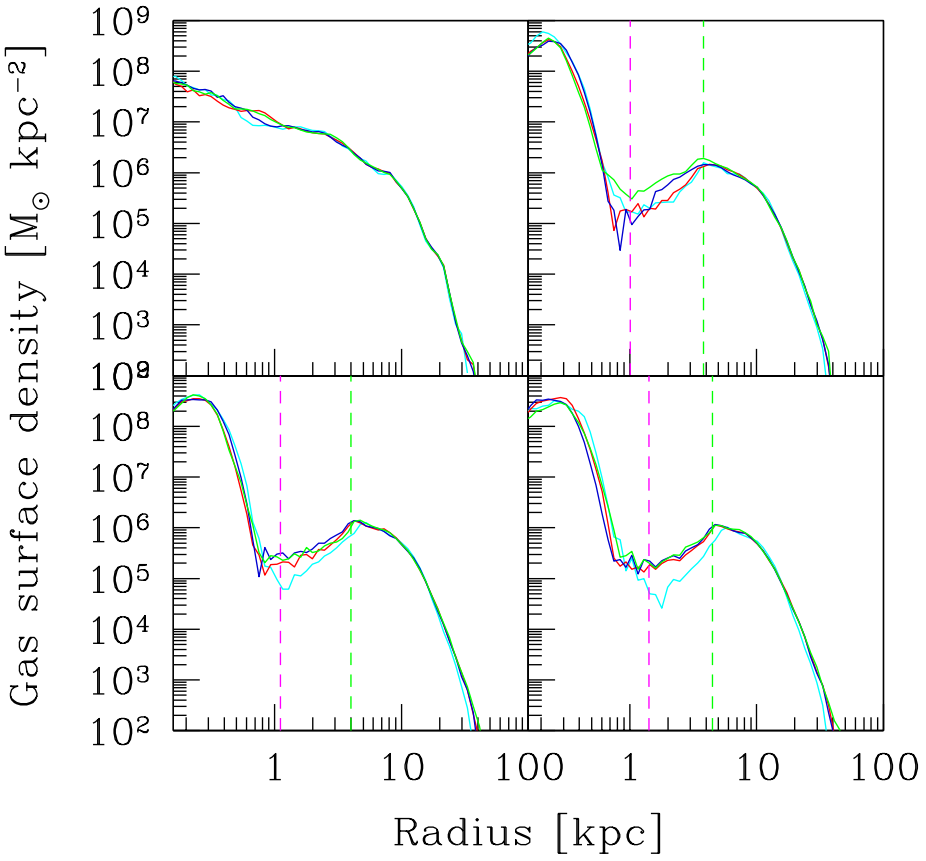

Figure 5.4: *LR simulation.* Surface density profile for low resolution isothermal simulations with different viscosity. Upper left, upper right, lower left and lower right panels refer to $t = 1$, 3, 5 and 7 Gyr, respectively. The solid red, green and blue curves are obtained from the gas particle distribution for simulation with $\alpha = 0.8$ (run LR), $\alpha = 1.6$ (run LRV16) and $\alpha = 0.4$ (run LRV04). The cyan curve corresponds to the gas particle distribution for simulation using GIZMO (LRGiz). The dashed magenta and green lines mark the positions of $R_{\rm ILR}$ and $R_{\rm C}$ at the different times.

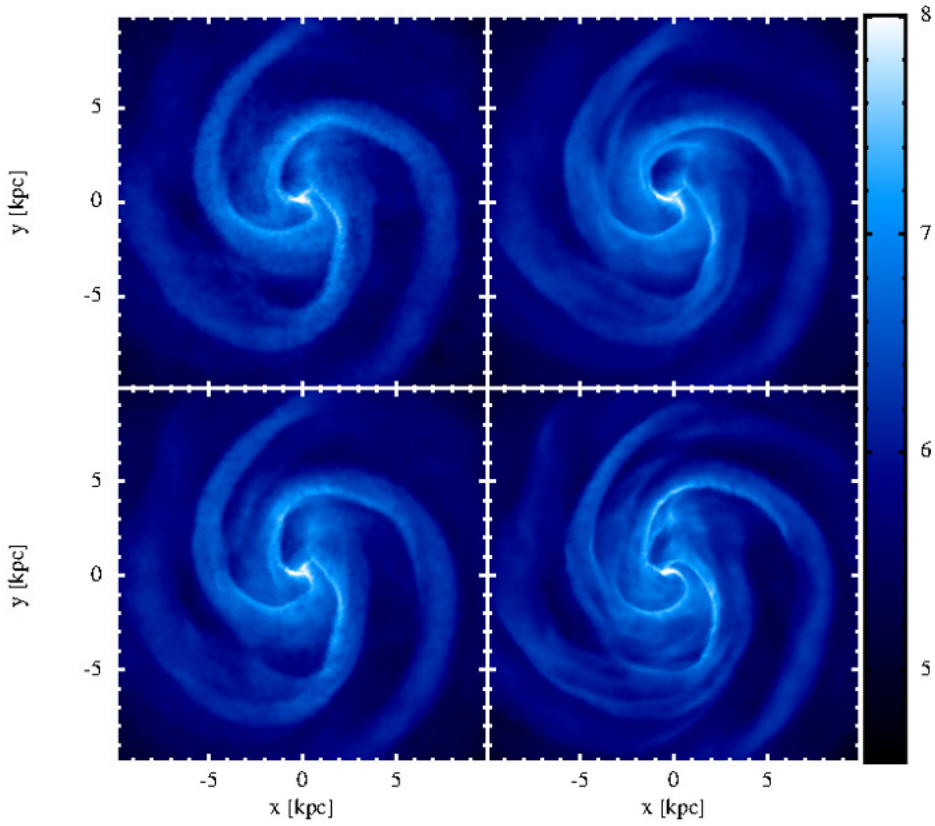

Figure 5.5: *LR simulation.* Logarithmic face-on views (in units of $M_\odot$ kpc^{-2}) of gas surface density for low resolution simulations with different values of α at t=1 Gyr: α=0.4 in the left upper panel, α=1.6 in the right upper panel, α=0.8 in the left lower panel and low resolution simulation using GIZMO in the right lower panel.

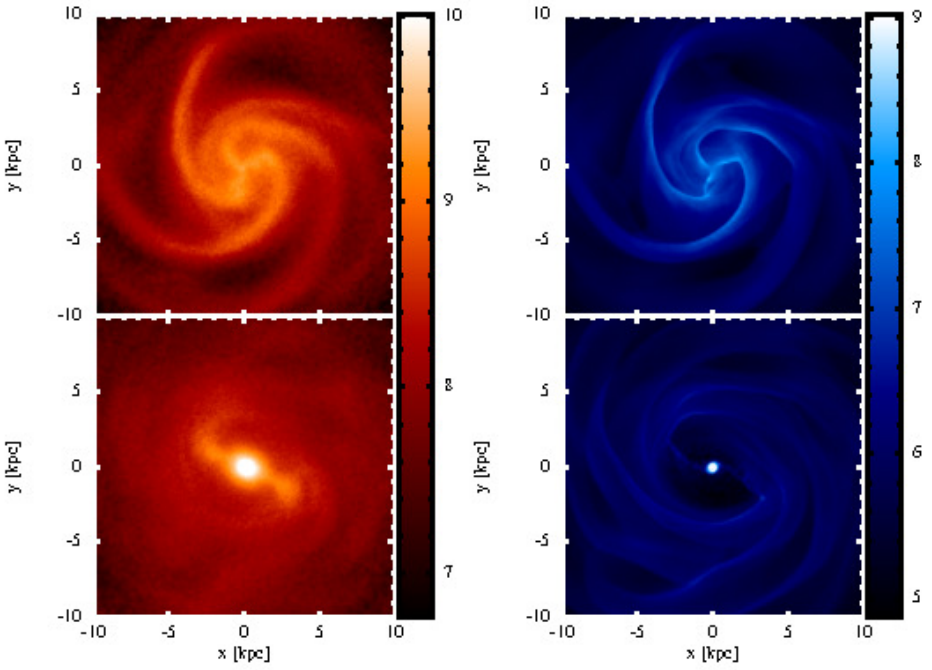

Figure 5.6: *HR simulation.* Right panels: logarithmic face-on views of the stellar surface density (in unit of $M_\odot$ kpc^{-2}) at $t = 1$ Gyr (upper panel) and $t = 2.5$ Gyr (lower panel). Left panels: same as right panels for the gas surface density.

the first evolutionary phase and being driven toward the centre during and after the bar formation. In the central region of the galaxy (within the bar extent) a "dead zone" forms, with very low density gas present in between the outer disc and the nuclear gas knot.

Figure 5.7 shows a comparison between HR and LR runs. The upper panel shows the gas surface density profiles in the two runs for four different times. The biggest difference is observable at $t \approx 1$ Gyr, when in the low resolution run (dashed lines) the disc is already significantly perturbed, while in the HR run (solid lines) the gas profile is still quite

unperturbed. The gas profile in the high resolution run is more similar to its low resolution analogous at later times, but for a slightly more pronounced "dead zone" in the HR run due to the better resolved profile of the stellar bar, that results in a more effective action of the bar itself onto the gas.

The main difference observed in the profiles at $t \approx 1$ Gyr is due to the later growth of non-axisymmetric perturbations (first in the form of spiral arms, turning into a central bar) in the higher resolution simulation. This is clearly observable in the accretion rate through the central 0.3 kpc (lower panel of Figure 5.7). In HR run the peak of $\dot{M}$ occurs at $t \approx 1.5$ Gyr, about 0.2-0.3 Gyr after the peak observed in the LR run. Again, in the high resolution simulation the $\dot{M}$ peak has a larger intensity (by almost a factor of 2) with respect to the low resolution case, due to the more efficient cleaning of the "dead zone" during the bar formation process.

The later growth of non-axisymmetric structures in the higher resolution run is probably due to the lower shot noise in the initial conditions: a higher number of particle MonteCarlo sampling results in a lower statistical noise, from which structures can grow (see also the discussion in Sellwood, 2014). An extensive and time consuming study aiming at numerical convergence is neither feasible (within the currently available computational facilities) nor useful, as a simulation with a order of magnitudes larger number of particles could result in a degree of symmetry significantly larger than any real disc galaxy observed. The dependence of the $\dot{M}$ peak and of the time at which spirals and bars form on the number of particles used demonstrate that these should not be taken as physical values. Only the gas response pattern is similar in all the runs analysed, independently on the viscosity prescription adopted, of the numerical resolution achieved, and of the algorithm used to solve the gas dynamics.

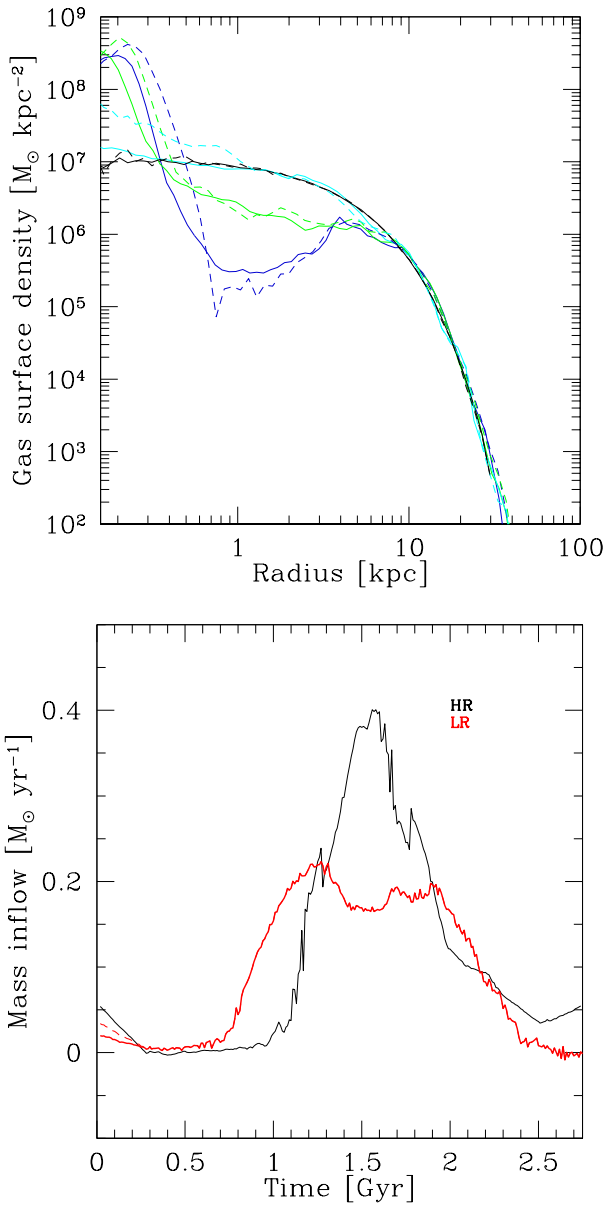

Figure 5.7: *LR and HR simulations.* Upper panel: surface density profile of the gas. Solid lines refer to the highest resolution run HR. The results of the low resolution run LR are reported with dashed lines for comparison. Black, cyan, green and blue curves refer to t =0, 1, 2, and 3 Gyr, respectively. Lower panel: gaseous mass inflow as a function of time. Black and red lines represent the inflow rate computed at 0.3 kpc from the center in run HR and LR, respectively.

Dynamics of the nuclear inflow

The high resolution achieved allows us to resolve sub-kpc scales, and to investigate the detailed causes of the nuclear gas inflow through the search of stellar and gaseous nuclear structures. In this section I focus on two times, just before (0.8 Gyr) and right at the beginning (1.1 Gyr) of the major gas inflow event. The properties of the stellar and gaseous distribution at the two times are highlighted in the upper and lower panels of Figure 5.8.

The left panels represent the surface density contrast for the stars within the inner 3 kpc, defined as:

$$\delta_{\Sigma_\star}(R,\phi) = \frac{\Sigma_\star(R,\phi) - \langle\Sigma_\star(R,\phi)\rangle_\phi}{\langle\Sigma_\star(R,\phi)\rangle_\phi}, \tag{5.1}$$

where R and ϕ are the radial and azimuthal coordinates on the disc equatorial plane, $\Sigma_\star(R,\phi)$ is the stellar surface density and $\langle\Sigma_\star(R,\phi)\rangle_\phi$ is the average stellar surface density evaluated in annuli. The central panels show the gas density contrast

$$\delta_{\rho,\mathrm{gas}}(R,\phi) = \frac{\rho_{\mathrm{gas}}(R,\phi) - \langle\rho_{\mathrm{gas}}(R,\phi)\rangle_\phi}{\langle\rho_{\mathrm{gas}}(R,\phi)\rangle_\phi}, \tag{5.2}$$

evaluated on the disc mid-plane. The right panels show the intensity of the radial motions.

Before the major inflow event (upper left panel) a single three arm spiral structure is visible down to scales of about 300 pc. The gas is affected by the stellar non-axisymmetric structure and develops shocks at the edge of the stellar spirals, as observable in density contrast map (upper central panel). Clear shock fronts develop in the gas distribution, the gas dynamics is perturbed and radial motions are triggered (upper right panel).

A different picture is present at the triggering of the strong gas inflow

episode (lower panels). At $t = 1.1$ Gyr the inner part (within ≈ 1 kpc) of the stellar three arm spiral structure decouples from the outer spiral structure, still evident at large scales (~ 3 kpc), as clearly visible in the lower left panel. Such decoupled structure is clearly observable in the gas density (lower central panel) map. The interplay between the outer and inner spiral structure increases the radial velocity of the gas in the central regions as well as the region participating to the radial inflow (lower right panel). By the time a clear bar forms, all the gas affected by the nuclear spirals formed the central nuclear knot.

Nuclear disc

I devoted the last part of the analysis to the structure of the gas nuclear system forming during the major inflow event. In particular I focused on the gas properties well after the nuclear structure formed and reached a stable configuration.

Figure 5.9 shows the density contrast of gas in the inner 3 kpc (left panel) and in the inner 400 pc (middle panel), and the radial velocity map (right panel) at about 2.5 Gyr. The orientation of the bar is traced by the inflowing streams of gas that connect the outer regions of the galaxy with the inner gaseous structure. The gas in the inner few hundreds of pc forms a rotating disc. Within the disc nuclear spirals are observable down to few tens of pc, traced by local gaseous overdensities (lighter regions in the central panel) corresponding to inflowing gas (blue and green regions in the right panel). A careful analysis of the stellar distribution does not show any central structure (neither in the form of spirals nor of bar). I therefore interpret the central two armed spirals as the effect that the outer bar has onto the gas within its ILR, as discussed analytically in Maciejewski (2004a) and observed in numerical simulations of the response of gas to a bar-like analytical potential (Maciejewski, 2004b).

As a note of caution I stress that the accretion rate at late times and,

more in general, the long-term evolution of the central gaseous concentration would be significantly different if the gas would be allowed to form stars, possibly forming a pseudo-bulge like structure.

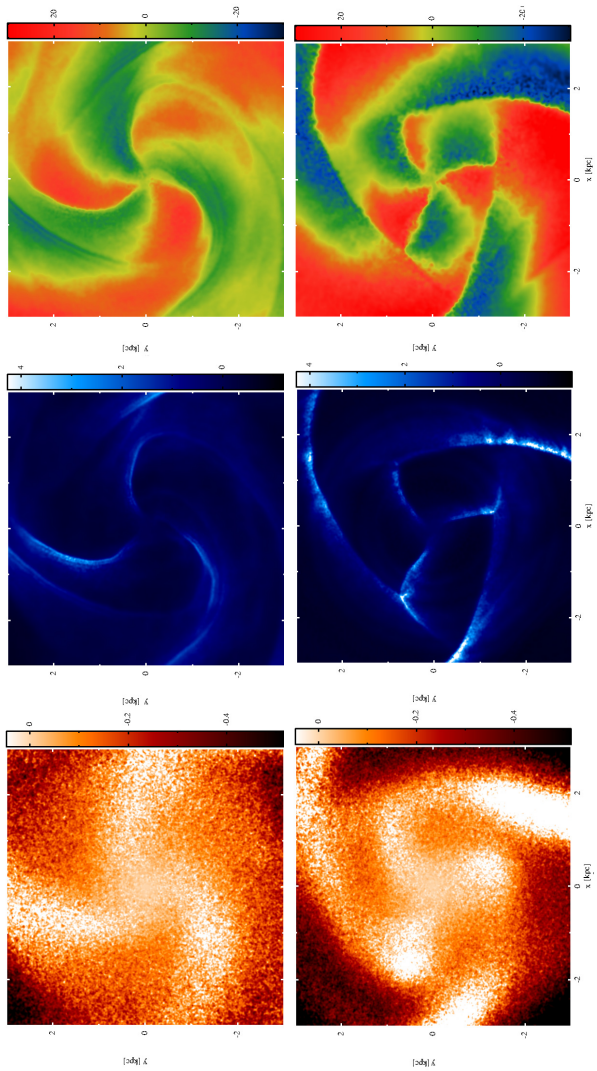

Figure 5.8: *HR simulation.* Upper panels: stellar surface density contrast (left), gas density contrast (middle) and radial velocity map (right) for gas in the inner 3 kpc at t =0.8 Gyr. Lower panels: same as the upper panels at t = 1.1 Gyr. See text for details.

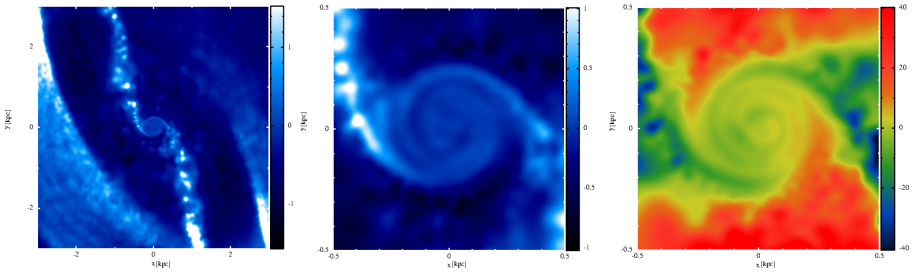

Figure 5.9: *HR simulation.* Gas density contrast in the inner 3 kpc (left panel) and 500 pc (central panel). The right panel shows the radial velocity for gas in the inner 500 pc at 2.5 Gyr. See text for details.

5.2 Cooling-star formation and stellar feedback runs

5.2.1 Low resolution simulation (LRPh)

I used the code GIZMO (Hopkins, 2014) including the implementations of star formation, cooling and stellar feedback to simulate a new suite of runs of the bar-unstable disc (see Section 4.2 for details). Similarly to previous sections, Figure 5.10 shows the distribution of stellar and gas disc observed in the LRPh run at three different times, $t = 1$, 4 and 7 Gyr in the left, central and right panels respectively. The stellar surface density is shown in the upper and middle panels (edge-on and face-on views, respectively). During the first 2 Gyr the bar-unstable system evolves from an axisymmetric configuration to a barred disc, passing through the formation of three arm spiral structure (visible in the stellar distribution at $t = 1$ Gyr in the left-middle panel of Figure 5.10). At about $t = 2$ Gyr, the disc presents a clear bar structure (with a diameter size of ≈ 8 kpc) in its central region. From 4 Gyr on, the bar thickens and buckles in its centre, as observable in the edge-on views of the stellar disc at $t = 4$ and 7 Gyr. At the end of the simulation a boxy-peanut bulge like structure is observable

within the central few kpc from the centre.

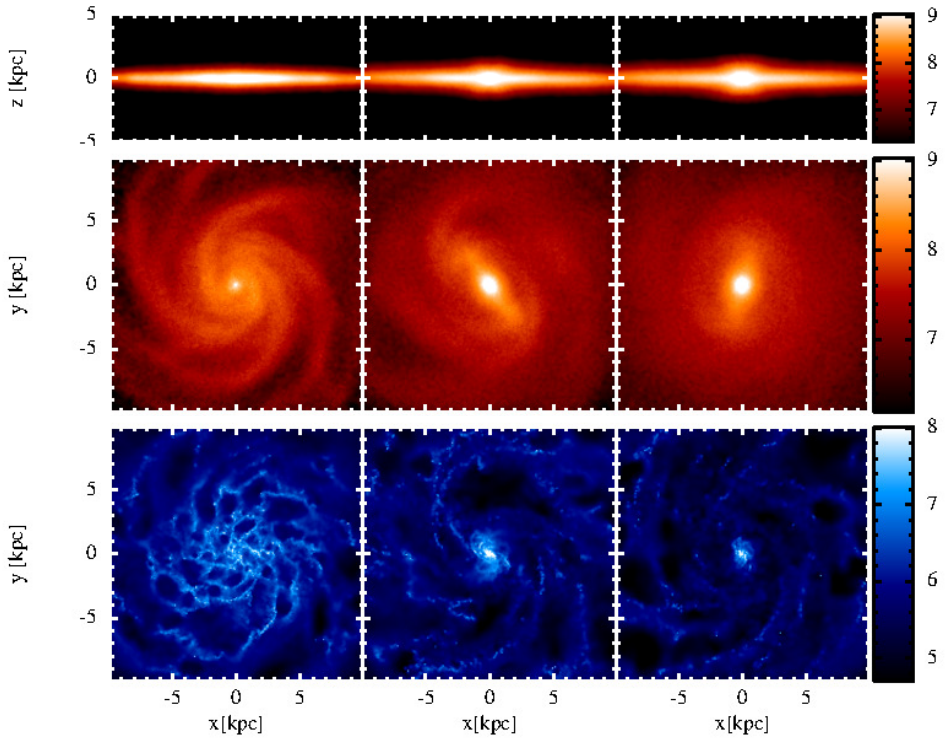

Figure 5.10: *LRPh simulation.* Upper (middle) panels: edge-on (face-on) views of the stellar disc at t =1, 4 and 7 Gyr (left, central and right panel, respectively). The colour gradient maps the stellar surface density (in units of $M_\odot$ kpc^{-2}) on a logarithmic scale. Bottom panels, same as the middle panel for the gas surface density.

The dynamics of the subdominant gas component is dominated by two processes: the underlying stellar dynamics and star formation. The face-on view of the gas surface density is shown in the lower panels. As in the previous case, the gas is affected by the stellar structures forming

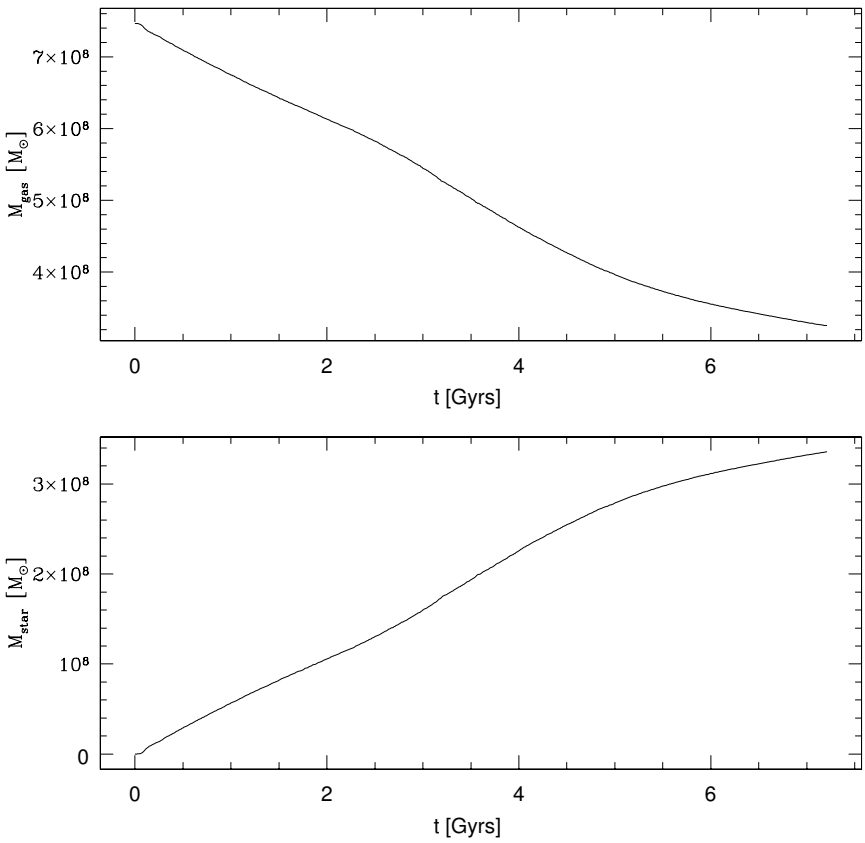

Figure 5.11: *LRPh simulation.* Upper panel: mass of gas in $M_\odot$ as a function of time. Lower panel: mass of new stars in $M_\odot$ as a function of time.

in the disc. However, in the gas distribution blast waves are also evident, due to the supernovae explosions. Then, the disc is significantly perturbed respect to the first suite of runs. When the bar is formed, the gas is driven toward the galaxy centre, forming a dense knot of gas clearly observable in the central and right panels in the bottom row of Figure 5.10. At

the same time, the gas is subjected to cooling processes which remove the thermal support resulting in high density structures, enforcing star formation. Figure 5.11 represents the mass of gas (upper panel) and new stars (lower panel) as a function of time. During the evolution, an increase of the star component corresponds to a gas component decrement.

The upper panel of Figure 5.12 quantifies the effect that the bar formation process has onto new stars (red lines) and gas (blue lines) at different time with respect to the gaseous disc at initial condition (magenta dashed line). The black line in figure represents the surface density profile of the sum of new stars and gas. In particular, gas density profiles increase up to ≈ 1 order of magnitude from $t = 1$ to 5 Gyr in the centre of the galaxy because of the influence of the bar potential on particles. New stars density profiles increase up to ≈ 1 order of magnitude from $t = 1$ to 5 Gyr, too. Such a central enhance of the newly formed star density is caused by the gas migration toward the inner regions of the galaxy, where a fraction of it is transformed in new stars.

Differently from the first set of simulations presented in section 5.1, most of the gas inflow happens at ≈ 3 Gyr, when the bar is a stable structure, as shown in the gas accretion rate $\dot{M}$ in the inner 0.3 kpc as a function of time, in the lower panel of Figure 5.12. We can also notice that the peak of $\dot{M}$ is lower respect to the isothermal simulations. This might mean that physical processes like star formation and stellar feedback could hinder or delay the inflow of gas to the center of galaxy. In particular, peaks and drops are visible: the latter correspond to high temperature in the inner region of the disc caused by recent SNae explosions, where the high pressure halts the inflowing gas. In the extreme case where the pressure overcomes gravity, the gas is swept outwards. Due to the high density in the central region, radiative cooling is particularly efficient in reducing gas temperature (and pressure as well) and this leads to a new phase of gas inflow, represented by peaks.

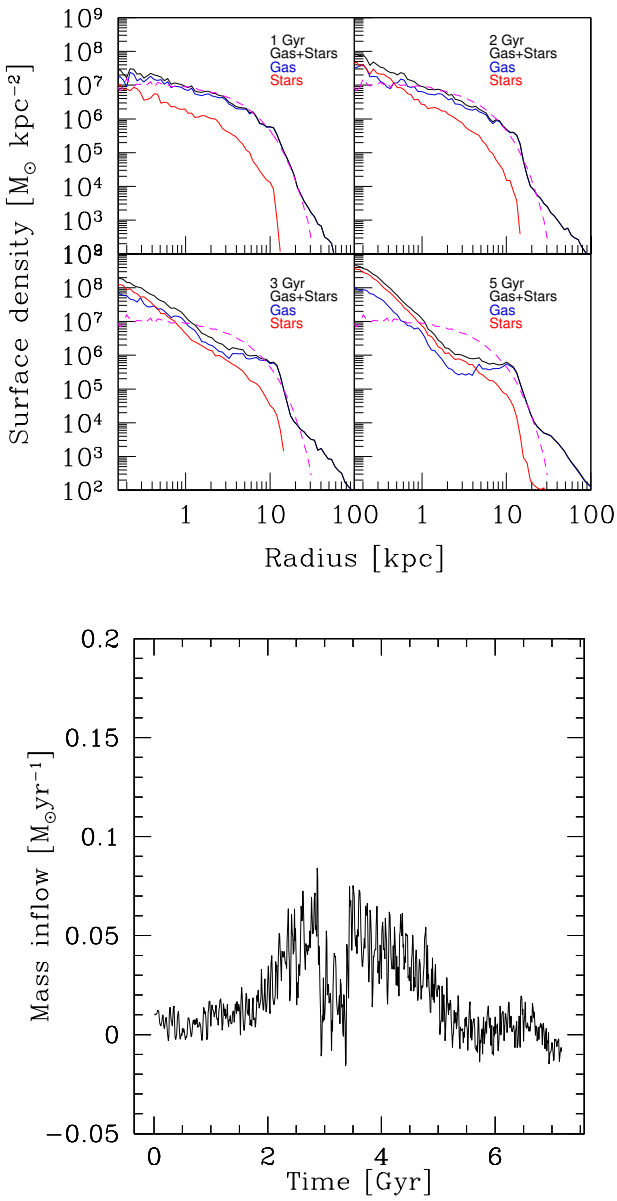

Figure 5.12: *LRPh simulation.* Upper panel: Surface density profile of the gaseous component (blue lines) and new stellar component (red lines) at t =1, 2, 3, and 5 Gyr, respectively. The black lines correspond to the surface density profile of the sum of new stars and gas. The magenta dashed lines represent the gaseous disc at initial conditions. Lower panel: gaseous mass inflow as a function of time within 0.3 kpc from the center.

5.2.2 High resolution simulation (HRPh)

For comparison, I run an high resolution version of the LRPh simulation (HRPh). Figure 5.13 shows the edge-on and face-on views of stellar (upper-middle panels) and gaseous (lower panels) surface density at $t =$ 1, 4 and 7 Gyr. Similarly to the low resolution simulation, during the first Gyr, the system develops stellar spiral arms (middle left panel) which evolve in a stable bar like structure at about 2 Gyr. The gas follows a similar dynamics as observed in the lower resolution run, along the stellar spiral arms, driven toward the central region of the galaxy.

The upper panel of Figure 5.14 presents the surface density profiles of new stars (red lines) and gas (blue lines) at different time respect to the gaseous disc at initial condition (magenta dashed line). The stellar and gas density profile increase up to ≈ 1 order of magnitude from $t = 1$ to 5 Gyr. The black line in figure represents the surface density profile of the sum of new stars and gas. Comparing this figure to Figure 5.12, it is evident that there are no significant differences: the trends of gas and new stars are completely in agreement with the low resolution simulation.

Similarly to the LRPh simulation, most of the gas inflow happens at ≈ 3 Gyr, when the bar is a stable structure, as shown in the lower panel of Figure 5.14. This delay in the gas inflow respect to the HR simulation (lower panel of Figure 5.7) could be due by the presence of feedback and star formation which hide and hinder the inflow of gas, as explained in the analysis of LRPh simulation.

To study the distribution of new stars respect to the stellar disc, I consider stars formed during the evolution of the system. Figure 5.15 shows the face-on and edge-on view of stellar density at $t = 1$, 2, 3 and 5 Gyr. The contours of new stellar component are placed on and it is possible to notice that they faithfully follow the trend of old stellar disc. A natural consequence is that stellar discs distributions (both the original and the new stellar disc) are purely dependent on the bar potential rather

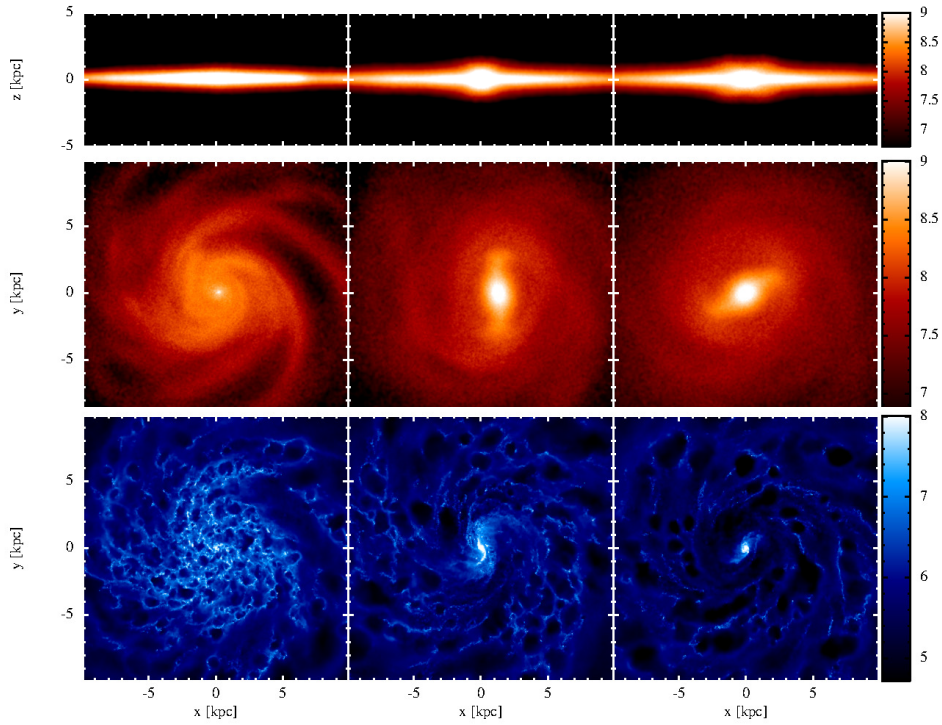

Figure 5.13: *HRPh simulation.* Upper (middle) panels: edge-on (face-on) views of the stellar disc at t =1, 4 and 7 Gyr (left, central and right panel, respectively). The colour gradient maps the stellar surface density (in units of $M_\odot$ kpc^{-2}) on a logarithmic scale. Bottom panels, same as the middle panel for the gas surface density.

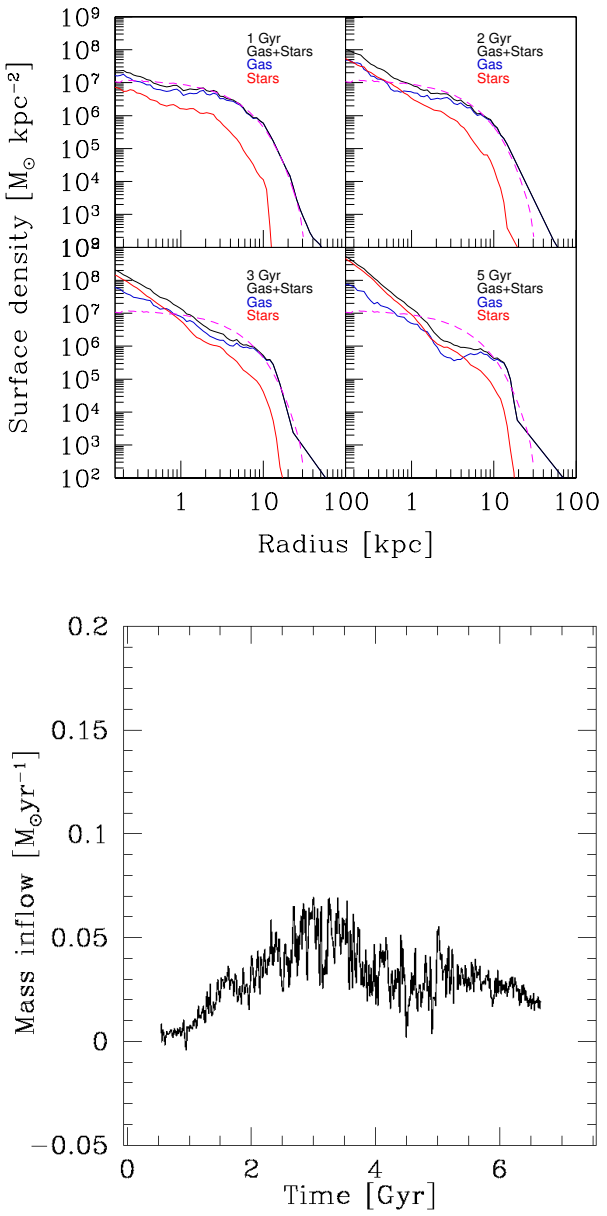

Figure 5.14: *HRPh simulation.* Upper panel: surface density profile of the gaseous component (blue lines) and stellar component (red lines) at t =1, 2, 3, and 5 Gyr, respectively. The black lines corresponds to the surface density profile of the sum of new stars and gas. The magenta dashed lines represents the gaseous disc at initial conditions. Lower panel: gaseous mass inflow as a function of time within 0.3 kpc from the center.

then any physical processes implemented in the system.

Nuclear disc

Similarly to the previous section, I analyse the structure of the gas nuclear system forming during the major inflow event. Figure 5.16 shows the density contrast of gas in the inner 3 kpc (left panel) and radial velocity map (right panel) at about 2.5 Gyr for gas in HRPh simulation. These images are quite different compared with the Figure 5.9: the gas in the centre does not form a clear disc. However, the orientation of the bar is traced by weak overdensities (lighter regions in the left panel) in the gas density contrast, more visible in the radial velocity map corresponding to the gas inflow (blue and green regions). The lack of nuclear structures is probably due to the presence of physical processes like cooling and star formation which perturb the system.

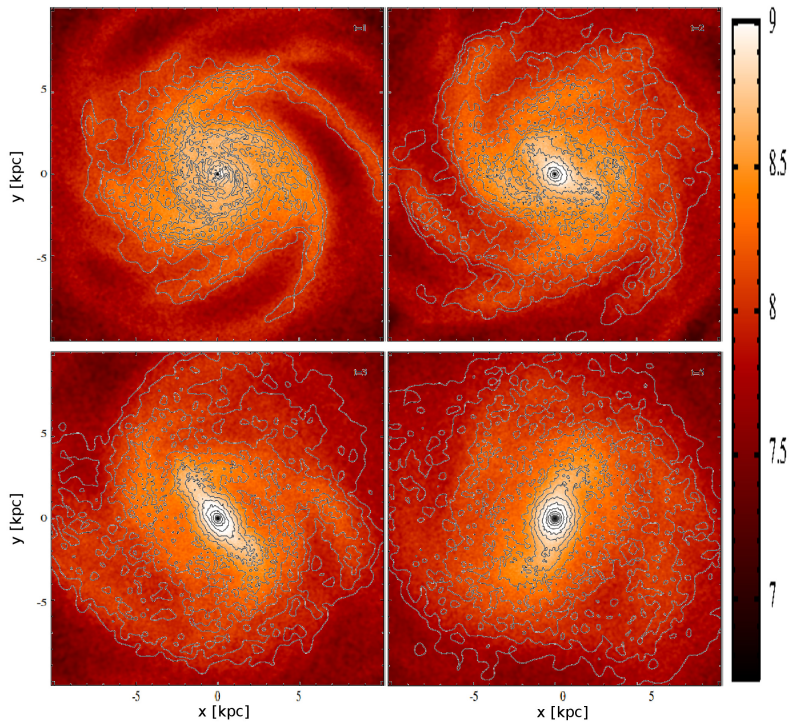

Figure 5.15: *HRPh simulation.* Face-on views of the stellar disc at t =1, 2, 4 and 5 Gyr. The colour gradient maps the stellar surface density (in units of $M_\odot$ kpc^{-2}) on a logarithmic scale. The black contours represent the new stars surface density.

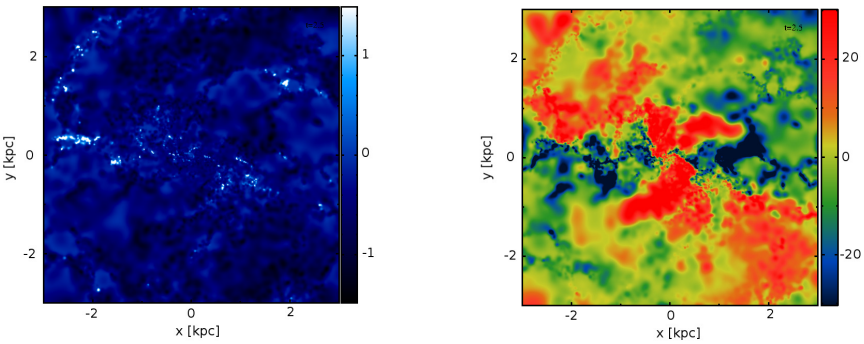

Figure 5.16: *HR simulation.* Gas density contrast (left panel) and radial velocity for gas in the inner 3 kpc at 2.5 Gyr. See text for details.

5.3 Boxy-peanut bulge

As I have already shown, the evolution of the systems proposed in the previous sections presents three different phases: during the first 2 Gyr the stellar disc evolves from an axisymmetric configuration to a barred disc, passing through the formation of transient multi-arm spirals. From 2 Gyr on the disc shows a clear bar structure in its central region and from 4 Gyr the bar tends to slow-down and buckles in its centre in a boxy-peanut bulge like structure. This structure is easily recognizable in the upper right panels of Figure 5.1, 5.10 and 5.13 which represent the edge-on views of the stellar disc at t =7 Gyr. It is interesting to study the distribution of new stars formed during the evolution of the system, respect to the stellar disc. Figure 5.17 shows the edge-on views of the system at t = 1, 2, 3 and 5 Gyr (from upper left to lower right panel). Each panel is composed of two images: the first represents the stellar

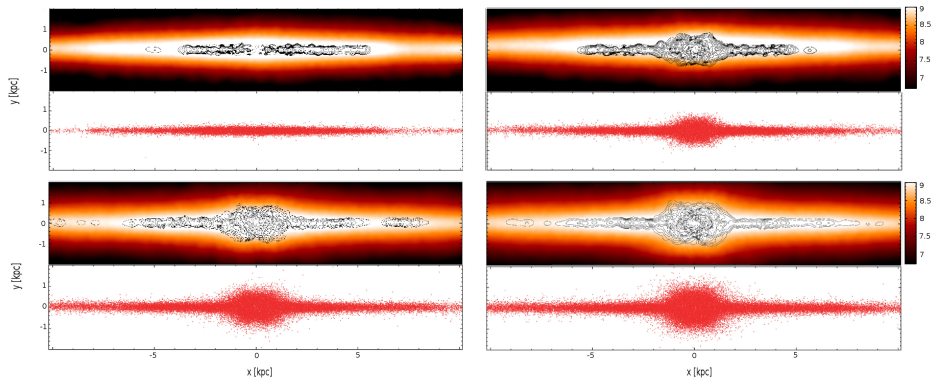

Figure 5.17: *HRPh simulation.* Edge-on views of the stellar disc at t =1, 2, 4 and 5 Gyr. The colour gradient maps the stellar surface density (in units of $M_\odot$ kpc^{-2}) on a logarithmic scale. The black contours represent the new stars surface density.

density and the contours of new stellar disc are placed on in black. The second represents the distribution of new stellar component, in red. From this figure it is possible to notice that in addition to following the trend of stellar disc, new stars faithfully trace the boxy-peanut bulge like structure, influenced by the presence of the bar potential which causes 3D orbits, far form the disc plane.

An other way to identify the boxy-peanut bulge like structure is to analyse the x-z projection (edge-on, with the bar perpendicular to the line of sight) as follows: I computed their x coordinates to calculate the median height of stars from the disc plane. This result is plotted in Figure 5.18: the two peaks corresponds to the over-densities due to the boxy-peanut bulge.

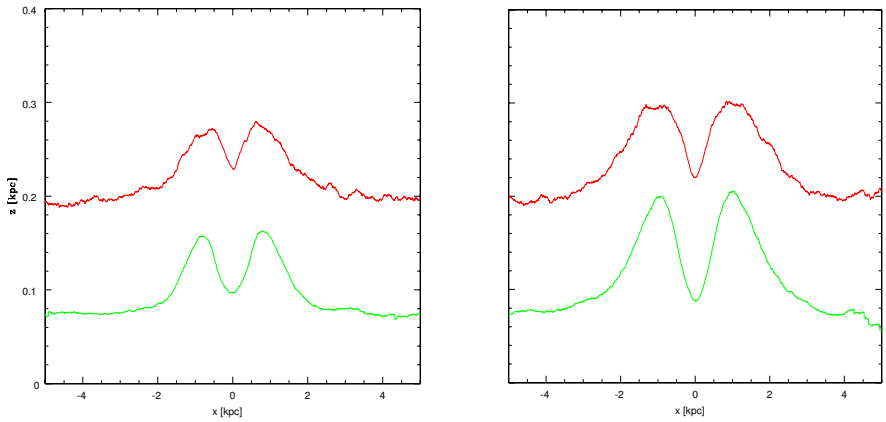

Figure 5.18: *HRPh simulation.* Median height of stars from the disc plane. The red line corresponds to old stars, the green line corresponds to new stars at $t = 5$ Gyr (left panel) and $t = 7$ Gyr (right panel).

CHAPTER 6

CONCLUSIONS

In this work I studied the gas response to the formation and evolution of a stellar bar in an isolated disc galaxy. Bars have been proven to be good candidates as responsible for the feeding mechanisms needed to transport mass in the central region of galaxies and trigger the consequent inner star formation. The simulation of this kind of system is very interesting to better understand the physical dynamics of bars and their effects on the other galactic components.

In the models, the galaxy is an un-barred isolated galactic disc, composed of stars and gas embedded in an evolving dark matter halo. This system is initially unstable to the formation of non-axisymmetric structures. First, I run simulations without the implementation of gas radiative cooling, star formation and stellar feedback prescriptions in order to test the basic numerical method used and the physical and dynamical effect of the forming substructures onto the gas (Isothermal simulations). Then, I run the same system implementing the physical processes mentioned above and I compare the corresponding results with the first set of sim-

ulations (Cooling star-formation and stellar feedback simulations). Both simulation suites have low and high resolution configurations, depending on the number of particles involved.

Isothermal runs

The system evolves for ≈ 7 Gyr. During this time I distinguished three different phases in the behaviour of stellar and gaseous disc evolution:

- **the stellar disc** is bar-unstable and during the first 2 Gyr evolves from an axisymmetric configuration to a barred disc, passing through the formation of transient multi-arm spirals (at about 1 Gyr). From 2 Gyr on, the disc shows a clear bar structure extended from the center of about 4 kpc in radius. From the bar formation time on (2 Gyr), the bar tends to slow-down, decreasing its frequency. In this phase, the bar forms thin and buckles in its center developing a boxy-peanut bulge like structure in the central few kpc of the disc, visible in the edge-on view of the system.

- **the gaseous disc**, forced by the stellar potential, is dominated by the underlying stellar dynamics. During the first 2 Gyr the gas distribution is similar to the stellar one and presents clear spiral arms co-spatial with the stellar ones. Then, the gas within the bar corotational radius ($4 - 5$ kpc from the center) is driven toward the galaxy center and forms a dense knot of gas. The torquing effect of the spiral arms before and the stellar bar afterwards sweeps the almost totality of the gas between the corotational radius and the central dense knot, except for two inflowing streams connecting the outer galactic disc with the central dense knot, often observed in real galaxies (Regan et al., 1999).

I checked the results against the numerical viscosity used, and I demonstrated that the gas dynamics is little affected by the exact value of the viscosity parameter in the SPH runs, and by the exact hydrodynamical treatment of the gas. I also studied the dependence of the results on the numerical resolution. I found that, although the qualitative evolution of the gas is resolution independent, the exact time at which the non axisymmetric structures develop and the actual maximum inflow rate at small (but completely resolved) scales do depend on the resolution achieved. As discussed above, the difference in the timescales for the inflow and for the bar formation are probably due to a lower shot noise in the highest resolution initial conditions. The difference in the magnitude of the maximum inflow rate, instead, is due to the fact that the bar itself as well as all the non-axisymmetric structure are better resolved in the highest resolution run, resulting in a more effective torquing of the gas.

The main result from this set of simulations consists in the efficiency of the "dead zone", such as the internal region depleted of gas. Most of the inflow in this region happens during the first 2 Gyr, when the bar is not completely formed yet. The fully formed bar does indeed play a role in further decreasing the gas surface density in the "dead zone" and in preventing new gas to refill the central regions by pushing the gas immediately outside the corotational radius toward the outer Lindblab resonance radius. However, it is instead the formation of the bar which is efficient in driving substantial gas inflow. In this phase the major episode of gas inflow takes place, larger by a factor of $\gtrsim 3$ than any other inflow event after the bar formation. The analysis of the higher resolution simulation shows that the trigger of the major inflow is the decoupling of the nuclear regions of the three armed spiral from the outer counterpart. At later times, when the stellar bar is already established, a low gas density annulus (here defined as the dead zone) between the bar corotational radius and the inner Lindblad resonances $R_{\rm ILR} \lesssim R \lesssim R_{\rm C}$ is clearly observable

in the simulations. The "dead zone" described above is often observed in local samples of barred spiral galaxies, as extensively discussed in Gavazzi et al. (2015). In Figure 6.1 three snapshots of the stellar and gas surface densities for HR simulation at t=1, 4 and 9 Gyr are shown in the central columns with three images of real galaxies (NGC 3596, NGC 5921, NGC 5701 from top to bottom) for comparison. Although this simulation does not include any prescription for star formation, the extreme gas density in the nucleus and its short dynamical time ensures that most of the gas mass is must be converted into stars in a burst on nuclear star formation, likely resulting in the formation of a pseudobulge. After the short transient starburst event, the gas density and the star formation rate drops. At ≈ 9 Gyr, the stellar bar has swept the quasi-totality of the gas within the corotational radius and the simulation reproduces the properties of a centrally quenched galaxy as NGC 5701. This study demonstrates that the central regions of barred galaxies are, on average, quenched with respect to the corresponding outer parts.

The explanation of such result is twofold: (1) since bars are quite efficient in driving the gas within their corotational radius toward the centre, after few bar orbits the central region of the galaxy is mostly gas free (as already noted by Berentzen et al., 1998), and there is no remaining gas to be torqued by the bar; (2) in the simulations the forming bar slows down as the galaxy evolves, increasing its ILR and corotational radii (in agreement with, e.g. Sellwood, 1981; Combes and Sanders, 1981; Halle et al., 2015). As a consequence, the gas that is perturbed by the early fast-precessing bar reaches regions significantly more nuclear than gas perturbed at later times. The low efficiency of large, long-lived and easy to spot bars in fuelling the very central regions of galaxies can explain why many observational studies do not find significant links between bars and AGN activity. The high efficiency of the *bar formation* process in driving strong inflows toward the very central region of galaxies hints, on

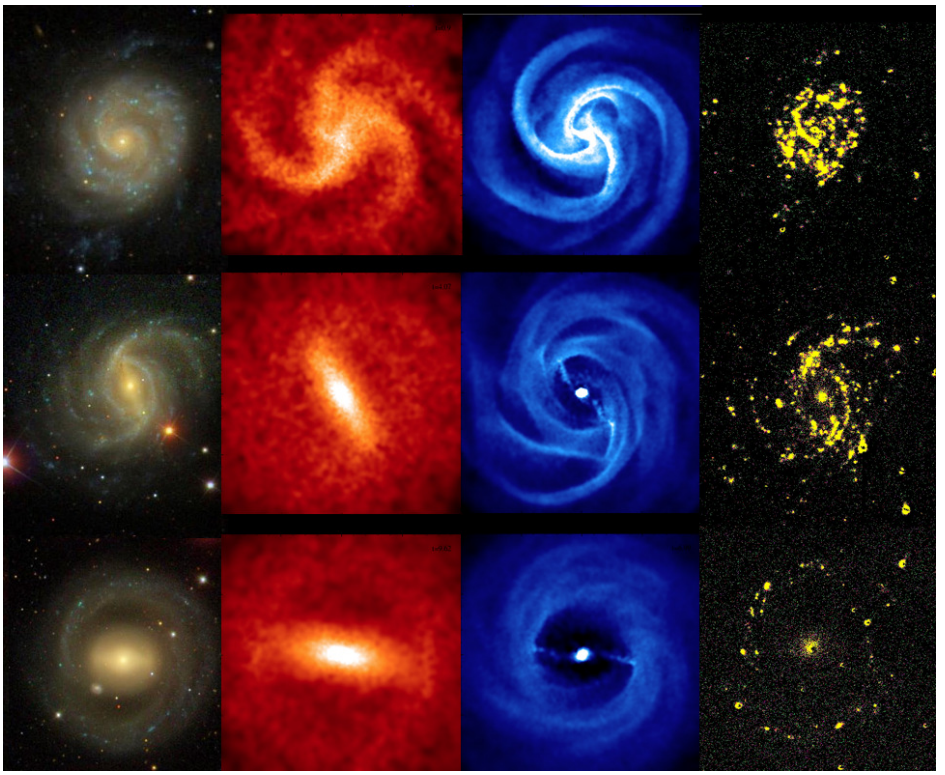

Figure 6.1: Left column: RGB images (SDSS) of three galaxies with increasing stellar mass (NGC 3596, NGC 5921, NGC 5701 from top to bottom) showing a regular spiral galaxy (top), a well-developed bar (middle), a barred ring (bottom). Second and third columns: face-on views of HR simulations of stars and gas densities from t=1 to t=4 Gyr showing a spiral disc galaxy (top) that becomes bar unstable (middle). Inside the corotation radius, the gas in conveyed towards the center and quickly consumed. Outside the corotational radius, the gas is unperturbed and feeds peripheral star formation. At the latest step (7 Gyr), the galaxy fully develops the bar and the central region is completely evacuated of gas. A ring of gas is left outside and feeds the star formation, as confirmed by the righ column showing Hα images. When the bar is well developed (two bottom panels), the star formation is suppressed inside the bar cotorational radius, but it is ongoing in the outer parts. From Gavazzi et al. (2015).

the other hand, at a possibly underestimated importance of bar driven AGN activity in disc galaxies.

Finally, the analysis of the long lived nuclear gaseous disc shows that the outer, large scale, bar keeps on exerting a dynamical effect onto the gas within few hundreds of pc. A two armed spiral can be observed both in the gas density distribution and in the gas dynamics, as already discussed by Maciejewski (2004a) and Maciejewski (2004b).

As a final note, I used the results of the 3D runs (in particular the potential generated by the stellar and dark matter components) to build an analytical approximation of the barred disc potential. I then performed the analysis of a set of 2D runs in which the gas evolves isothermally under the effect of such analytical potential, and I checked that *i*) the results are similar to those obtained in the full 3D runs, and *ii*) that the gas evolution is mainly driven to the torques exerted by the bar onto the gas, intrinsically linked to the non-axisymmetric nature of the bar itself, and not the evolution of the (azimuthally averaged) radial profile of the potential (which does evolve in time during the bar formation and evolution). A full description of such test is presented in Appendix A.

Cooling-star formation and stellar feedback runs

The system evolves for ≈ 7 Gyr and I divided the evolution of the disc in three phases, similarly to the isothermal runs:

- the stellar disc history corresponds to the isothermal one: up to 2 Gyr it evolves from an axisymmetric configuration to a barred disc, passing through the formation of transient multi-arm spirals. Then, it presents a clear bar structure which elongates from the center for about 4 kpc and remains stable up to 4 Gyr when it buckles in its center and develops a boxy-peanut bulge like structure.

	Isothermal runs	**Physical runs**
Phase 1 (t< 2 Gyr)	STARS: spiral arms GAS: spiral arms	STARS: spiral arms GAS: clumpy distribution
Phase 2 (2 <t< 4 Gyr)	STARS: bar GAS: "dead zone"	STARS: bar GAS: "dead zone"
Phase 3 (4 <t< 7 Gyr)	STARS: boxy-peanut GAS: "dead zone"	STARS: boxy-peanut GAS: "dead zone"

Table 6.1: Main features for the two set of simulation in the three different phases of evolution.

- the gaseous disc distribution is quite different from the stellar one. Already in the first 2 Gyr the gas does not follow the spiral arms clearly visible in the stellar disc component. It is subjected to physical phenomena such as cooling, star formation and stellar feedback which perturbed its distribution hiding any possible formation of non-axisymmetric structures (e.g. spiral arms). The effect of the bar is still evident, especially after 2 Gyr, when the distribution of gas is very similar to the isothermal case: within the corotational radius, it is driven toward the galaxy center and forms a dense knot of gas. The region between this overdensity and the corotational radius is empty by the torquing effect of the spiral arms and the bar. The gas, subjected to the star formation process and conveyed to the center of the galaxy, heats and partially transforms in new stars. For this reason, at the end of the simulation the central overdensity is weaker then in the second phase and part of the gas has been replaced by new stars.

A comparison of the main features observed in the isothermal and physical runs are summarized in Table 6.1.

Similarly to the isothermal runs, I checked the dependence of the results on the numerical resolution and I found that the development of

different structures does not depend on it. The main difference from the previous set of runs consists in the time at which the gas inflow takes place: most of the gas inflow happens during the second phase, between 2 and 4 Gyr, when the bar is completely formed. Compared to the isothermal runs, the implementation of physical phenomena such as cooling, star formation and stellar feedback seems to affect the behaviour of gas and its distribution in the system, hindering and delaying the inflow toward the center of the galaxy. The evolution of this kind of simulations is subject to several variables which tune the physical processes implemented. Different values of such parameters could lead to different results. At the present stage of investigation we cannot discriminate between the two following scenarios: *i*) the runs implementing radiative cooling and star formation related physics do represent a good description of the real evolution of an isolated spiral galaxy undergoing bar instability. In this case the above-mentioned parameters (set in agreement with previously published investigation at significantly coarser resolution (Hopkins, 2014)) and the feedback associated with the stellar evolution keeps the gas supported during the first phase of bar formation; *ii*) the effect of stellar feedback is overestimated in the physical runs, and the actual parameters that would properly reproduce the evolution of an isolated galaxy in simulations at pc-scale resolution have to be constrained starting from a comparison between the results of high-resolution runs and observations resolving similar scales. This second possible scenario would explain why the gas morphology and dynamics in the isothermal runs traces so well the properties of gas and star formation in real barred galaxies in the local Universe (Gavazzi et al., 2015). I plan to perform a detailed study of the effect of the implemented physics and a thorough comparison with observations in a future investigation.

APPENDIX A

2D SIMULATIONS

In this chapter I analyse the potential which influences gas particles in 3D simulations discussed above and I find an analytical function to describe it.

A.1 Potential fit

Gas particles are subjected to an axisymmetric potential from dark matter halo and disc components, and a non-axisymmetric potential due to the bar. As a result, the total potential is defined as:

$$\Phi_{\rm tot} = \Phi_{\rm (DM+disc)}(R) + \Phi_{\rm bar}(R, \varphi). \tag{A.1}$$

as explained in eq. 2.20. Figure A.1 shows the total potential of stellar disc for the LR simulation during the evolution of the system: green and blue points correspond to the potential at initial condition (before the bar formation) and 4 Gyr (after the bar formation). The red line corresponds to the theoretical potential trend of dark matter halo. Before the bar

a [km^2/s^2]	b [km^2/s^2]	c [km^2/s^2]	d [kpc^{-1}]	f
$-3.471 \cdot 10^4$	$-3.631 \cdot 10^4$	$-1.754 \cdot 10^4$	$6.212 \cdot 10^{-3}$	$7.437 \cdot 10^{-2}$

Table A.1: Coefficient values for theoretical dark matter-disk potential (eq. A.2) at every time.

formation (green points) the stars potential is in agreement with the theoretical one because the disc is essentially dominated by the dark matter halo and the bar is not present. After the bar formation (blue points) the stars potential change its trend, especially at small radius. This is different from the theoretical prediction because of the presence of the bar which exerts its non-axisymmetric potential on the particles up to its corotational radius, at about 4 kpc from the center.
At every time, the contribution of dark matter and disc is well fitted by a quadratic logarithmic transform 2D function:

$$\Phi_{\mathrm{DM+disk}}(R) = \mathrm{a} + \mathrm{b}[\ln(\mathrm{d}R + \mathrm{f})] + \mathrm{c}[\ln(\mathrm{d}R + \mathrm{f})]^2, \qquad (A.2)$$

where R is the radius and coefficient values are listed in Table A.1.
By subtracting this function to the total potential of stars, I obtain the remaining radial dependence of bar potential. Similarly to the contribution of dark matter and disc, I fit this component to describe the radial potential of bar with an analytical relation, such as the double exponential function:

$$\Phi_{\mathrm{bar}}(R) = \mathrm{g}\exp(\mathrm{l}R) + \mathrm{m}\exp(\mathrm{n}R). \qquad (A.3)$$

Coefficient values at different time are listed in Table A.2. I limit the fit to the corotational radius of the bar, since out of this radius the force of the bar is flat and the dark matter-disc component dominates the potential. In Figure A.2, left panels show the total potential at 4 and 7 Gyr from stars (black points) and $\Phi_{\mathrm{DM+disc}}$ fit (green points). Right panels represent the bar potential from stars (black points) and the corresponding fit (red

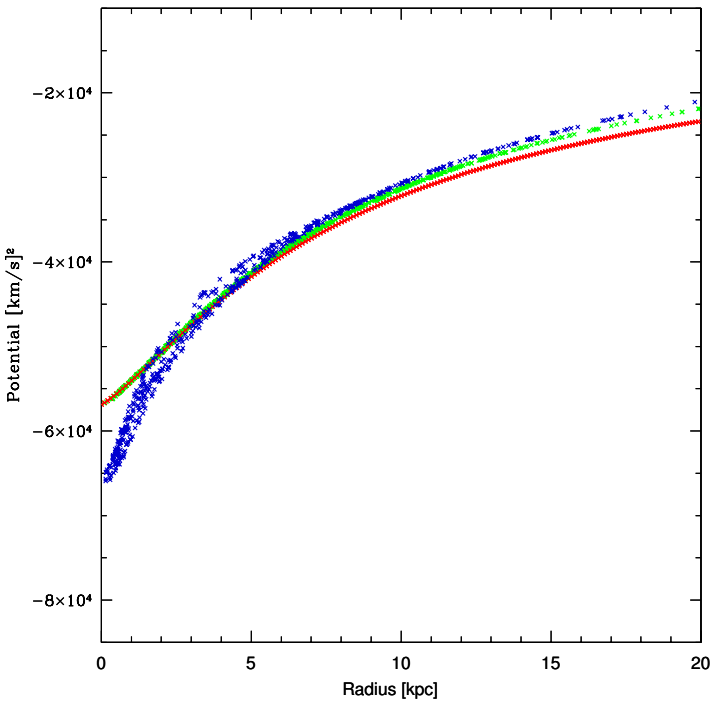

Figure A.1: *LR simulation.* Potential of particles: green and blue points correspond to the potential of stars at initial condition and 4 Gyr. The red line corresponds to the theoretical potential from dark matter halo.

t [Gyr]	g [km^2/s^2]	l [kpc^{-1}]	m [km^2/s^2]	n [kpc^{-1}]
4	$1.027 \cdot 10^7$	$-1.599 \cdot 10^{-1}$	$-1.028 \cdot 10^7$	$-1.602 \cdot 10^{-1}$
7	$1.178 \cdot 10^4$	$-5.409 \cdot 10^{-2}$	$-3.106 \cdot 10^4$	$-2.490 \cdot 10^{-1}$

Table A.2: Coefficient values for theoretical bar potential (eq. 5) at 4 and 7 Gyrs.

points).

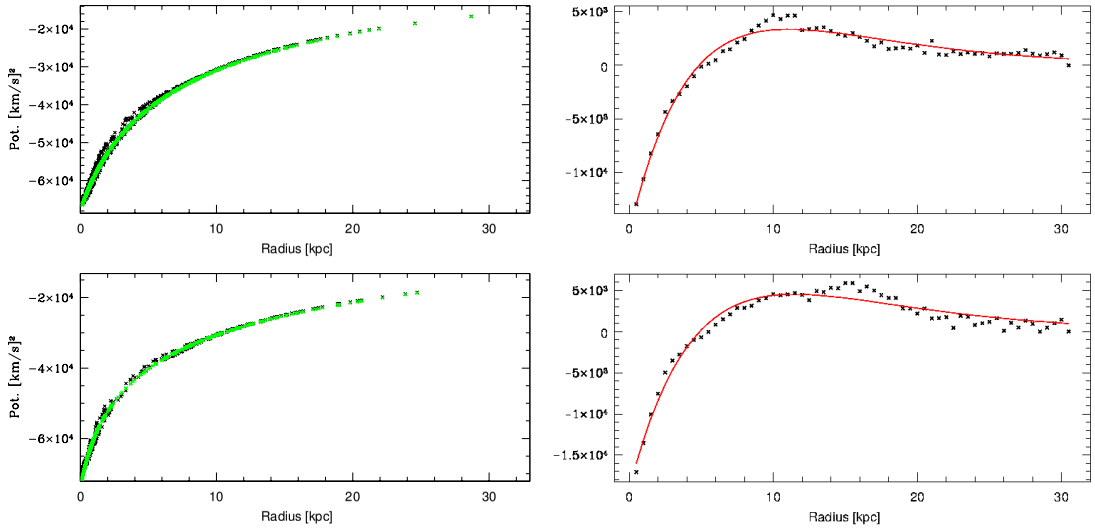

Figure A.2: Total potential of particles (left panels) at 4 and 7 Gyr: black points represent total potential from simulation and green points correspond the potential fit (eq. A.2). Bar radial potential (right panels) at 4 and 7 Gyr: black points represent the bar potential from simulation and red points correspond to the bar potential fit (eq. A.4).

The bar potential is non-axisymmetric, then it has an angular dependence. In this work I use the Sanders et al. (1977) formalism, so the bar potential can be finally written as:

$$\Phi_{\rm bar}(R,\phi) = [\mathrm{g}\ \exp(\mathrm{l}R) + \mathrm{m}\ \exp(\mathrm{n}R)]\cos 2(\varphi - \Omega_{\rm bar}t), \tag{A.4}$$

where $\Omega_{\rm bar}$ is the angular frequency of the bar.

A.2 Simulation suite

I simulate 2D gaseous disk, in order to test the influence of potentials fitted in the previous section. The disc is modelled as a radial exponential disc from Hernquist (1993) (see Section 4.1 for more details) with a radial scale length of 3 kpc and a vertical scale length of 0.3 kpc. The gas component has the same mass of previous simulations, it has a uniform temperature $T_0 = 10000$ K and evolves isothermically. This system is composed of $5 \cdot 10^4$ gas particles with a softening length of 15 pc and it evolves using the smoothed particle hydrodynamics (SPH) code Gadget2 (Springel 2005) for about 7 Gyr. The accelerations implemented on the code are directly derivable from the potential equations A.2 and A.4:

$$\boldsymbol{a} = \frac{\mathrm{d}\boldsymbol{\Phi}_{\rm tot}}{\mathrm{d}\boldsymbol{R}} + \frac{\mathrm{d}\boldsymbol{\Phi}_{\rm tot}}{\mathrm{d}\varphi} \tag{A.5}$$

The evolution of the system is composed by different phases:

- up to 1 Gyr the disc evolves dominated by dark matter potential and the umperturbed disc which remains constant for all the simulation

evolution;

- from 1 to 2 Gyr the bar is forming: the bar potential grows linearly with time;
- from 2 to 4 Gyr the bar is formed and is a stable structure;
- from 4 to 5 Gyr the bar linearly grows to form its final stage: the boxy peanut bulge;
- from 5 the bar stops growing and becomes a stable structure again.

A.3 Results

I find the fits for the contribution of disc-dark matter and bar potentials. I run the gaseous system described to study the inflow of gas subjected to the fitted potentials and compare results with those in the isothermal simulation. Figure A.3 represents the face-on distribution of gas observed at three different times, $t = 1$, 3 and 5 Gyr on the left, central and right panels respectively. During the first 2 Gyr, the system is subjected to the disc-dark matter potential and to the growing bar potential. The gas responds to these components with the formation of 2 weaks spiral arms. After 2 Gyr the bar potential remains stable and the gas inside the corotational radius (setted at 4 kpc) is driven toward the galaxy center and forms an overdensity evident in the central and right panels. The influence of the bar sweeps the gas between the corotational radius and the central dense knot.

The Figure A.4 shows the surface density profile of gas. Solid black, cyan, green, blue and yellow curves are obtained from the gas particle distribution at $t = 0$, 1, 2, 3 and 5 Gyr, respectively. Comparing this figure with the left panel of Figure 5.3 it is possible to notice that gas inflows are very similar in the two different cases: at small radius the

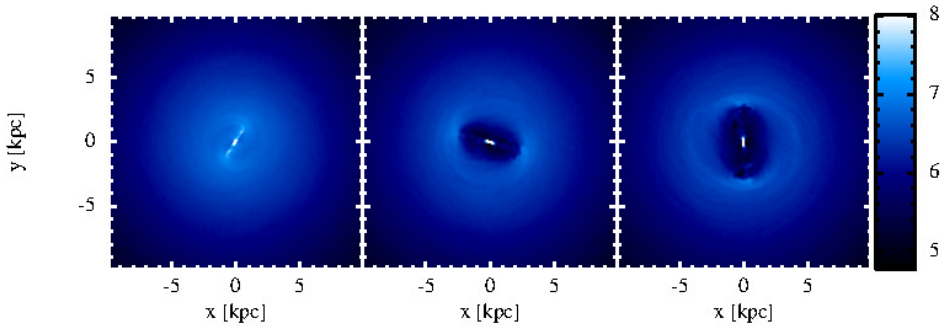

Figure A.3: Surface density profile in the 2D simulation of a gaseous disc subjected to disc-dark matter and bar potential described in eq. A.2 and A.4 at 1 Gyr (left panel), 3 Gyr (central panel) and 5 Gyr (right panel).

surface density increases form the initial condition (black line) to the end of evolution (red line). The most gas inflow happens between 1 and 2 Gyr (cyan and green lines). I can conclude that the total potential from eq. A.2 and A.4 is a good fit to describe a system composed by a gaseous disk subjected to a bar component.

To verify that the visible gas inflow is due to the symmetry breaking introduced by bar component (and not simply due to the deepening of the central azimuthally averaged potential), I simulate the system implementing the disc-dark matter potential fit and the bar radial potential fit, excluding the angular part (eq. A.3). The Figure A.5 shows the surface density profile of gas. Solid black, cyan, green, blue and yellow curves are obtained from the gas particle distribution at $t = 0$, 1, 2, 3 and 5 Gyr, respectively. I can compare this figure with Figure A.4 and notice that the gas inflow is very different: at small radius the gas surface density does not increase. This can be explained by the lack of the angular component in the bar potential implementation which causes torques on gas and support the inflow toward the center of the galaxy.

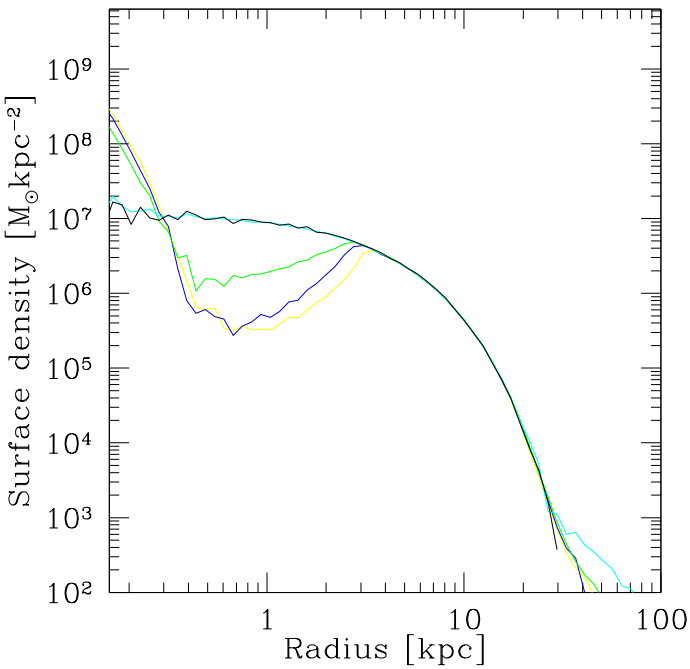

Figure A.4: Surface density profile in the 2D simulation of a gaseous disc subjected to disc-dark matter and bar potential described in eq. A.2 and A.4. The solid black, cyan, green and blue curves are obtained from the gas particle distribution at t=0, 1, 2, 3 and 5, respectively.

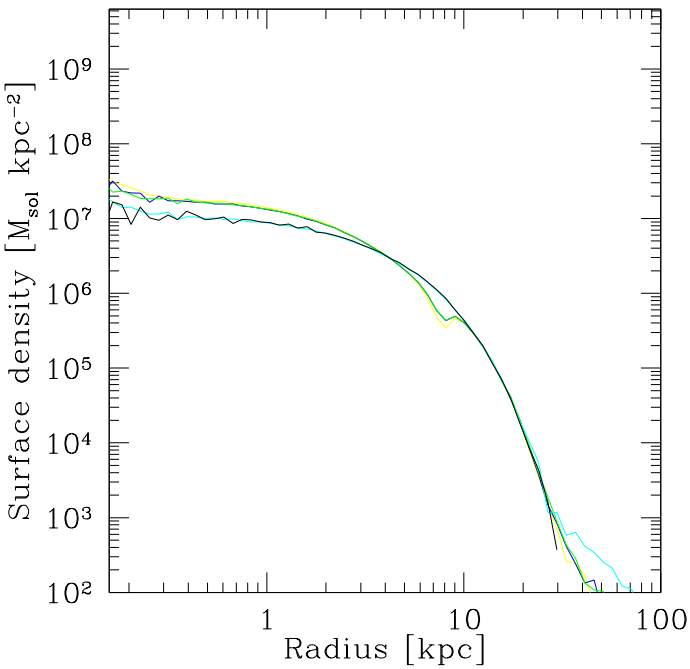

Figure A.5: Surface density profile in the 2D simulation of a gaseous disc subjected to disc-dark matter and bar potential described in eq. A.2 and A.3. The solid black, cyan, green and blue curves are obtained from the gas particle distribution at t=0, 1, 2, 3 and 5, respectively.

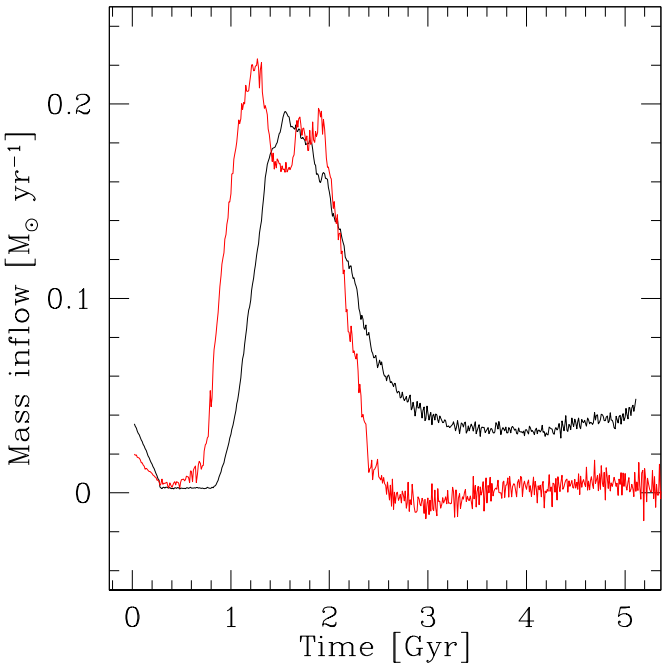

Figure A.6: Gaseous mass inflow as a function of time. Black line represents the accretion rate computed at 0.3 kpc from the center, while the red line corresponds to the LR simulation trend in the same range.

To quantify the gas inflow visible in Figure A.4, I plot the gas accretion rate $\dot{M}$ as a function of time in Figure A.6. The black line refers to $\dot{M}$ throught surfaces at 0.3 kpc from the centre for the 2D simulation discussed above, while the red line corresponds to the LR simulation in the same range, for comparison. The plot shows a prominent peak between 1 and 2 Gyr, during the linear growing of the bar potential, then the trend weakens progressively during the evolution, according with the LR simulation proceeding.

A.4 2D vs 3D

Comparing the gaseous systems in Figure 5.1 and Figure A.3, I can make some considerations. First of all, it is inevitable to have differences in the distribution of gas between 2D and LR simulations: in the LR run, I consider a gaseous disc subjected to the influence of a bar unstable stellar component. In this case, the dynamics of the gas is dominated by the underlying stellar dynamics. Conversely, in the 2D run, the gas is subjected to the implementation of the bar potential fit derived from LR simulation. In spite of it can be considered a good approximation, it depends on distinct parameters, such as the different values listed in Table A.1 and A.2 and on the different phases chosen for the evolution of the system.

Anyway, especially in the second part of the evolution (after 2 Gyr), the two simulations are very similar to each other: both present a clear overdensity in the center of the disc and a cleaning zone inside the corotational radius, evidence of the presence of the bar that sweeps the almost totality of the gas in this region. Similarly to LR run, in the 2D simulation the gas surface density and the mass inflow rate present a peak fully comparable with those in the LR one.

From these analysis I can conclude that the equations A.2 and A.4 represent quite closely the effect that a bar has on the gas, therefore they can be considered a good approximation to describe a gaseous disc subjected to bar instability.

LIST OF TABLES

LIST OF FIGURES

BIBLIOGRAPHY

M. S. Alonso, G. Coldwell, and D. G. Lambas. Effect of bars in AGN host galaxies and black hole activity. A&A, 549:A141, January 2013. doi: 10.1051/0004-6361/201220117.

A. W. Appel. An Efficient Program for Many-Body Simulation. *SIAM Journal on Scientific and Statistical Computing, vol. 6, no. 1, January 1985, p. 85-103.*, 6:85–103, January 1985.

E. Athanassoula. The spiral structure of galaxies. Phys. Rep., 114:319–403, 1984. doi: 10.1016/0370-1573(84)90156-X.

E. Athanassoula. The existence and shapes of dust lanes in galactic bars. MNRAS, 259:345–364, November 1992.

E. Athanassoula. What determines the strength and the slowdown rate of bars? MNRAS, 341:1179–1198, June 2003. doi: 10.1046/j.1365-8711.2003.06473.x.

E. Athanassoula. Boxy/peanut/X bulges, barlenses and the thick part of

galactic bars: What are they and how did they form? *ArXiv e-prints*, March 2015.

D. S. Balsara. von Neumann stability analysis of smooth particle hydrodynamics–suggestions for optimal algorithms. *Journal of Computational Physics*, 121:357–372, 1995. doi: 10.1016/S0021-9991(95)90221-X.

J. Barnes and P. Hut. A hierarchical O(N log N) force-calculation algorithm. Nature, 324:446–449, December 1986. doi: 10.1038/324446a0.

I. Berentzen, C. H. Heller, I. Shlosman, and K. J. Fricke. Gas-driven evolution of stellar orbits in barred galaxies. MNRAS, 300:49–63, October 1998. doi: 10.1046/j.1365-8711.1998.01836.x.

I. Berentzen, I. Shlosman, I. Martinez-Valpuesta, and C. H. Heller. Gas Feedback on Stellar Bar Evolution. ApJ, 666:189–200, September 2007. doi: 10.1086/520531.

J. Binney and S. Tremaine. *Galactic Dynamics: Second Edition*. Princeton University Press, 2008.

S. Bonoli, L. Mayer, S. Kazantzidis, P. Madau, J. Bellovary, and F. Governato. Black Hole Starvation and Bulge Evolution in a Milky Way-like Galaxy. *ArXiv e-prints*, August 2015.

G. L. Bryan, M. L. Norman, B. W. O'Shea, T. Abel, J. H. Wise, M. J. Turk, D. R. Reynolds, D. C. Collins, P. Wang, S. W. Skillman, B. Smith, R. P. Harkness, J. Bordner, J.-h. Kim, M. Kuhlen, H. Xu, N. Goldbaum, C. Hummels, A. G. Kritsuk, E. Tasker, S. Skory, C. M. Simpson, O. Hahn, J. S. Oishi, G. C. So, F. Zhao, R. Cen, Y. Li, and Enzo Collaboration. ENZO: An Adaptive Mesh Refinement Code for Astrophysics. ApJS, 211:19, April 2014. doi: 10.1088/0067-0049/211/2/19.

G. Chabrier. Galactic Stellar and Substellar Initial Mass Function. PASP, 115:763–795, July 2003. doi: 10.1086/376392.

R. A. Chevalier. The Evolution of Supernova Remnants. Spherically Symmetric Models. ApJ, 188:501–516, March 1974. doi: 10.1086/152740.

M. Cisternas, D. A. Gadotti, J. H. Knapen, T. Kim, S. Díaz-García, E. Laurikainen, H. Salo, O. González-Martín, L. C. Ho, B. G. Elmegreen, D. Zaritsky, K. Sheth, E. Athanassoula, A. Bosma, S. Comerón, S. Erroz-Ferrer, A. Gil de Paz, J. L. Hinz, B. W. Holwerda, J. Laine, S. Meidt, K. Menéndez-Delmestre, T. Mizusawa, J. C. Muñoz-Mateos, M. W. Regan, and M. Seibert. X-Ray Nuclear Activity in S^4G Barred Galaxies: No Link between Bar Strength and Cooccurrent Supermassive Black Hole Fueling. ApJ, 776:50, October 2013. doi: 10.1088/0004-637X/776/1/50.

D. R. Cole, V. P. Debattista, P. Erwin, S. W. F. Earp, and R. Roškar. The formation of stellar nuclear discs in bar-induced gas inflows. MNRAS, 445:3352–3369, December 2014. doi: 10.1093/mnras/stu1985.

F. Combes and R. H. Sanders. Formation and properties of persisting stellar bars. A&A, 96:164–173, March 1981.

G. de Vaucouleurs. Revised Classification of 1500 Bright Galaxies. ApJS, 8:31, April 1963. doi: 10.1086/190084.

V. P. Debattista and J. A. Sellwood. Dynamical Friction and the Distribution of Dark Matter in Barred Galaxies. ApJ, 493:L5–L8, January 1998. doi: 10.1086/311118.

V. P. Debattista and J. A. Sellwood. Constraints from Dynamical Friction on the Dark Matter Content of Barred Galaxies. ApJ, 543:704–721, November 2000. doi: 10.1086/317148.

E. Emsellem, F. Renaud, F. Bournaud, B. Elmegreen, F. Combes, and J. M. Gabor. The interplay between a galactic bar and a supermassive black hole: nuclear fuelling in a subparsec resolution galaxy simulation. MNRAS, 446:2468–2482, January 2015. doi: 10.1093/mnras/stu2209.

S. M. Fall and G. Efstathiou. Formation and rotation of disc galaxies with haloes. MNRAS, 193:189–206, October 1980.

R. Fanali, M. Dotti, D. Fiacconi, and F. Haardt. Bar formation as driver of gas inflows in isolated disc galaxies. MNRAS, 454:3641–3652, December 2015. doi: 10.1093/mnras/stv2247.

D. Fiacconi, R. Feldmann, and L. Mayer. The Argo simulation - II. The early build-up of the Hubble sequence. MNRAS, 446:1957–1972, January 2015. doi: 10.1093/mnras/stu2228.

E. Gaburov and K. Nitadori. Astrophysical weighted particle magnetohydrodynamics. MNRAS, 414:129–154, June 2011. doi: 10.1111/j.1365-2966.2011.18313.x.

G. Gavazzi, G. Consolandi, M. Dotti, R. Fanali, M. Fossati, M. Fumagalli, E. Viscardi, G. Savorgnan, A. Boselli, L. Gutiérrez, H. Hernández Toledo, R. Giovanelli, and M. P. Haynes. The role of bars in quenching star formation from z = 3 to the present epoch. Halpha3: an Halpha imaging survey of HI selected galaxies from ALFALFA, VI. *ArXiv e-prints*, May 2015.

R. A. Gingold and J. J. Monaghan. Smoothed particle hydrodynamics - Theory and application to non-spherical stars. MNRAS, 181:375–389, November 1977.

D. Goz, P. Monaco, G. Murante, and A. Curir. Properties of barred spiral disks in hydrodynamical cosmological simulations. *ArXiv e-prints*, December 2014.

A. Halle, P. Di Matteo, M. Haywood, and F. Combes. Quantifying stellar radial migration in a N-body simulation: blurring, churning, and the outer regions of galaxy discs. *ArXiv e-prints*, January 2015.

L. Hernquist. N-body realizations of compound galaxies. ApJS, 86:389–400, June 1993. doi: 10.1086/191784.

G. Hinshaw, D. Larson, E. Komatsu, D. N. Spergel, C. L. Bennett, J. Dunkley, M. R. Nolta, M. Halpern, R. S. Hill, N. Odegard, L. Page, K. M. Smith, J. L. Weiland, B. Gold, N. Jarosik, A. Kogut, M. Limon, S. S. Meyer, G. S. Tucker, E. Wollack, and E. L. Wright. Nine-year Wilkinson Microwave Anisotropy Probe (WMAP) Observations: Cosmological Parameter Results. ApJS, 208:19, October 2013. doi: 10.1088/0067-0049/208/2/19.

L. C. Ho, A. V. Filippenko, and W. L. W. Sargent. The Influence of Bars on Nuclear Activity. ApJ, 487:591–602, October 1997.

F. Hohl. Numerical Experiments with a Disk of Stars. ApJ, 168:343, September 1971. doi: 10.1086/151091.

P. F. Hopkins. GIZMO: A New Class of Accurate, Mesh-Free Hydrodynamic Simulation Methods. *ArXiv e-prints*, September 2014.

E. Hubble. No. 324. Extra-galactic nebulae. *Contributions from the Mount Wilson Observatory / Carnegie Institution of Washington*, 324:1–49, 1926.

E. P. Hubble. *Realm of the Nebulae*. 1936.

L. K. Hunt and M. A. Malkan. Morphology of the 12 Micron Seyfert Galaxies. I. Hubble Types, Axial Ratios, Bars, and Rings. ApJ, 516: 660–671, May 1999. doi: 10.1086/307150.

J. R. Hurley, O. R. Pols, and C. A. Tout. Comprehensive analytic formulae for stellar evolution as a function of mass and metallicity. MNRAS, 315: 543–569, July 2000. doi: 10.1046/j.1365-8711.2000.03426.x.

M. A. Jalali. Unstable Disk Galaxies. I. Modal Properties. ApJ, 669: 218–231, November 2007. doi: 10.1086/521523.

S. Jogee, N. Scoville, and J. D. P. Kenney. The Central Region of Barred Galaxies: Molecular Environment, Starbursts, and Secular Evolution. ApJ, 630:837–863, September 2005. doi: 10.1086/432106.

A. J. Kalnajs. The Equilibria and Oscillations of a Family of Uniformly Rotating Stellar Disks. ApJ, 175:63, July 1972. doi: 10.1086/151538.

R. C. Kennicutt, Jr. The Global Schmidt Law in Star-forming Galaxies. ApJ, 498:541–552, May 1998. doi: 10.1086/305588.

J.-h. Kim, T. Abel, O. Agertz, G. L. Bryan, D. Ceverino, C. Christensen, C. Conroy, A. Dekel, N. Y. Gnedin, N. J. Goldbaum, J. Guedes, O. Hahn, A. Hobbs, P. F. Hopkins, C. B. Hummels, F. Iannuzzi, D. Keres, A. Klypin, A. V. Kravtsov, M. R. Krumholz, M. Kuhlen, S. N. Leitner, P. Madau, L. Mayer, C. E. Moody, K. Nagamine, M. L. Norman, J. Onorbe, B. W. O'Shea, A. Pillepich, J. R. Primack, T. Quinn, J. I. Read, B. E. Robertson, M. Rocha, D. H. Rudd, S. Shen, B. D. Smith, A. S. Szalay, R. Teyssier, R. Thompson, K. Todoroki, M. J. Turk, J. W. Wadsley, J. H. Wise, A. Zolotov, and t. AGORA Collaboration29. The AGORA High-resolution Galaxy Simulations Comparison Project. ApJS, 210:14, January 2014. doi: 10.1088/0067-0049/210/1/14.

W.-T. Kim, W.-Y. Seo, and Y. Kim. Gaseous Structures in Barred Galaxies: Effects of the Bar Strength. ApJ, 758:14, October 2012. doi: 10.1088/0004-637X/758/1/14.

J. H. Knapen, I. Shlosman, and R. F. Peletier. A Subarcsecond Resolution Near-Infrared Study of Seyfert and "Normal" Galaxies. II. Morphology. ApJ, 529:93–100, January 2000. doi: 10.1086/308266.

E. Komatsu, K. M. Smith, J. Dunkley, C. L. Bennett, B. Gold, G. Hinshaw, N. Jarosik, D. Larson, M. R. Nolta, L. Page, D. N. Spergel, M. Halpern, R. S. Hill, A. Kogut, M. Limon, S. S. Meyer, N. Odegard, G. S. Tucker, J. L. Weiland, E. Wollack, and E. L. Wright. Seven-year Wilkinson Microwave Anisotropy Probe (WMAP) Observations: Cosmological Interpretation. ApJS, 192:18, February 2011. doi: 10.1088/0067-0049/192/2/18.

J. Kormendy. *Secular Evolution in Disk Galaxies*, page 1. October 2013.

K. Kraljic, F. Bournaud, and M. Martig. The Two-phase Formation History of Spiral Galaxies Traced by the Cosmic Evolution of the Bar Fraction. ApJ, 757:60, September 2012. doi: 10.1088/0004-637X/757/1/60.

S. Laine, I. Shlosman, J. H. Knapen, and R. F. Peletier. Nested and Single Bars in Seyfert and Non-Seyfert Galaxies. ApJ, 567:97–117, March 2002. doi: 10.1086/323964.

E. Laurikainen, H. Salo, and R. Buta. Comparison of Bar Strengths and Fractions of Bars in Active and Nonactive Galaxies. ApJ, 607:103–124, May 2004. doi: 10.1086/383462.

G.-H. Lee, C. Park, M. G. Lee, and Y.-Y. Choi. Dependence of Barred Galaxy Fraction on Galaxy Properties and Environment. ApJ, 745:125, February 2012a. doi: 10.1088/0004-637X/745/2/125.

G.-H. Lee, J.-H. Woo, M. G. Lee, H. S. Hwang, J. C. Lee, J. Sohn, and J. H. Lee. Do Bars Trigger Activity in Galactic Nuclei? ApJ, 750:141, May 2012b. doi: 10.1088/0004-637X/750/2/141.

G. Lodato and D. J. Price. On the diffusive propagation of warps in thin accretion discs. MNRAS, 405:1212–1226, June 2010. doi: 10.1111/j.1365-2966.2010.16526.x.

W. Maciejewski. Nuclear spirals in galaxies: gas response to an asymmetric potential - I. Linear theory. MNRAS, 354:883–891, November 2004a. doi: 10.1111/j.1365-2966.2004.08253.x.

W. Maciejewski. Nuclear spirals in galaxies: gas response to an asymmetric potential - II. Hydrodynamical models. MNRAS, 354:892–904, November 2004b. doi: 10.1111/j.1365-2966.2004.08254.x.

L. Martinet and D. Friedli. Bar strength and star formation activity in late-type barred galaxies. A&A, 323:363–373, July 1997.

L. Mayer and J. Wadsley. The formation and evolution of bars in low surface brightness galaxies with cold dark matter haloes. MNRAS, 347: 277–294, January 2004. doi: 10.1111/j.1365-2966.2004.07202.x.

R. H. Miller and B. F. Smith. Dynamics of a stellar bar. ApJ, 227:785–797, February 1979. doi: 10.1086/156787.

H. J. Mo, S. Mao, and S. D. M. White. The formation of galactic discs. MNRAS, 295:319–336, April 1998. doi: 10.1046/j.1365-8711.1998.01227.x.

J. J. Monaghan. Smoothed particle hydrodynamics. ARA&A, 30:543–574, 1992. doi: 10.1146/annurev.aa.30.090192.002551.

J. J. Monaghan. SPH and Riemann Solvers. *Journal of Computational Physics*, 136:298–307, September 1997. doi: 10.1006/jcph.1997.5732.

J. J. Monaghan and J. C. Lattanzio. A refined particle method for astrophysical problems. A&A, 149:135–143, August 1985.

J. S. Mulchaey and M. W. Regan. The Fueling of Nuclear Activity: The Bar Properties of Seyfert and Normal Galaxies. ApJ, 482:L135–L137, June 1997. doi: 10.1086/310710.

J. R. Murray. SPH simulations of tidally unstable accretion discs in cataclysmic variables. MNRAS, 279:402–414, March 1996.

P. B. Nair and R. G. Abraham. On the Fraction of Barred Spiral Galaxies. ApJ, 714:L260–L264, May 2010. doi: 10.1088/2041-8205/714/2/L260.

J. F. Navarro, C. S. Frenk, and S. D. M. White. The Structure of Cold Dark Matter Halos. ApJ, 462:563, May 1996. doi: 10.1086/177173.

J. F. Navarro, C. S. Frenk, and S. D. M. White. A Universal Density Profile from Hierarchical Clustering. ApJ, 490:493–508, December 1997.

S. Oh, K. Oh, and S. K. Yi. Bar Effects on Central Star Formation and Active Galactic Nucleus Activity. ApJS, 198:4, January 2012. doi: 10.1088/0067-0049/198/1/4.

J. P. Ostriker and P. J. E. Peebles. A Numerical Study of the Stability of Flattened Galaxies: or, can Cold Galaxies Survive? ApJ, 186:467–480, December 1973. doi: 10.1086/152513.

M. W. Regan and P. J. Teuben. Bar-driven Mass Inflow: How Bar Characteristics Affect the Inflow. ApJ, 600:595–612, January 2004. doi: 10.1086/380116.

M. W. Regan, K. Sheth, and S. N. Vogel. Molecular Gas Kinematics in Barred Spiral Galaxies. ApJ, 526:97–113, November 1999. doi: 10.1086/307960.

W. W. Roberts, Jr., J. M. Huntley, and G. D. van Albada. Gas dynamics in barred spirals - Gaseous density waves and galactic shocks. ApJ, 233: 67–84, October 1979. doi: 10.1086/157367.

E. Romano-Díaz, I. Shlosman, C. Heller, and Y. Hoffman. Disk Evolution and Bar Triggering Driven by Interactions with Dark Matter Substructure. ApJ, 687:L13–L16, November 2008. doi: 10.1086/593168.

K. Saha and O. Gerhard. Secular evolution and cylindrical rotation in boxy/peanut bulges: impact of initially rotating classical bulges. MNRAS, 430:2039–2046, April 2013. doi: 10.1093/mnras/stt029.

K. Saha, I. Martinez-Valpuesta, and O. Gerhard. Spin-up of low-mass classical bulges in barred galaxies. MNRAS, 421:333–345, March 2012. doi: 10.1111/j.1365-2966.2011.20307.x.

R. H. Sanders and J. M. Huntley. Gas response to oval distortions in disk galaxies. ApJ, 209:53–65, October 1976. doi: 10.1086/154692.

C. Scannapieco and E. Athanassoula. Bars in hydrodynamical cosmological simulations. MNRAS, 425:L10–L14, September 2012. doi: 10.1111/j.1745-3933.2012.01291.x.

J. A. Sellwood. Bar instability and rotation curves. A&A, 99:362–374, June 1981.

J. A. Sellwood. Secular evolution in disk galaxies. *Reviews of Modern Physics*, 86:1–46, January 2014. doi: 10.1103/RevModPhys.86.1.

I. Shlosman, J. Frank, and M. C. Begelman. Bars within bars - A mechanism for fuelling active galactic nuclei. Nature, 338:45–47, March 1989. doi: 10.1038/338045a0.

V. Springel. The cosmological simulation code GADGET-2. MNRAS, 364:1105–1134, December 2005. doi: 10.1111/j.1365-2966.2005.09655.x.

V. Springel and L. Hernquist. Cosmological smoothed particle hydrodynamics simulations: the entropy equation. MNRAS, 333:649–664, July 2002. doi: 10.1046/j.1365-8711.2002.05445.x.

V. Springel, N. Yoshida, and S. D. M. White. GADGET: a code for collisionless and gasdynamical cosmological simulations. New A, 6:79–117, April 2001. doi: 10.1016/S1384-1076(01)00042-2.

V. Springel, T. Di Matteo, and L. Hernquist. Modelling feedback from stars and black holes in galaxy mergers. MNRAS, 361:776–794, August 2005. doi: 10.1111/j.1365-2966.2005.09238.x.

G. Stinson, A. Seth, N. Katz, J. Wadsley, F. Governato, and T. Quinn. Star formation and feedback in smoothed particle hydrodynamic simulations - I. Isolated galaxies. MNRAS, 373:1074–1090, December 2006. doi: 10.1111/j.1365-2966.2006.11097.x.

A. Toomre. On the gravitational stability of a disk of stars. ApJ, 139: 1217–1238, May 1964. doi: 10.1086/147861.

J. Villa-Vargas, I. Shlosman, and C. Heller. Dark Matter Halos and Evolution of Bars in Disk Galaxies: Varying Gas Fraction and Gas Spatial Resolution. ApJ, 719:1470–1480, August 2010. doi: 10.1088/0004-637X/719/2/1470.

K. Wada. The Three-dimensional Structure of a Massive Gas Disk in the Galactic Central Region. ApJ, 559:L41–L44, September 2001. doi: 10.1086/323668.

K. Wada and C. A. Norman. Numerical Models of the Multiphase Interstellar Matter with Stellar Energy Feedback on a Galactic Scale. ApJ, 547:172–186, January 2001. doi: 10.1086/318344.

M. D. Weinberg. Evolution of barred galaxies by dynamical friction. MNRAS, 213:451–471, March 1985.

H. Wozniak and L. Michel-Dansac. Formation of young boxy/peanut bulges in ringed barred galaxies. A&A, 494:11–20, January 2009. doi: 10.1051/0004-6361:200810903.

A. Yoshino and C. Yamauchi. Box/peanut and bar structures in edge-on and face-on nearby galaxies in the Sloan Digital Sky Survey - I. Catalogue. MNRAS, 446:3749–3767, February 2015. doi: 10.1093/mnras/stu2249.

Questa tesi non é solo mia ma anche di tutti quelli che con me hanno condiviso questi tre anni, che con me hanno gioito e sofferto, soprattutto in questi ultimi folli mesi. Non faró nomi, ma sono sicura che leggendo queste poche righe c'é chi riuscirá a riconoscersi.

Grazie a chi mi ha dato sostegno nei momenti piú difficili (non solo a livello universitario), a chi ha condiviso con me i numerosi pranzi in auletta, a chi ha sopportato i miei dubbi esistenziali (spesso coincidenti con quelli informatici!!), a chi mi ha comprato il Maalox per tutto questo tempo e continua a comprarmelo, a chi mi ha fatto capire che non serve nessuna laurea per giocare all'"Identi-Peppa" e che continua ancora adesso a stracciarmi clamorosamente, a chi mi ha portato gelati, cioccolato e caramelle, a chi ha fatto le scale con me (e non per mantenersi in forma), a chi mi ruba la stufetta dall'ufficio ma appena arrivo me la riporta, a chi mi chiamava nel suo ufficio per farmi vedere esperimenti di fisica improvvisati sul momento o per raccontarmi le sue passeggiate, al Circolo del Caffé, a chi piace fare tanti scherzi al mio compagno di ufficio, a chi ha la faccia da pazza e a noi piace un sacco, a chi mi ha sfidato ripetutamente a Quiz Duello incapace di accettare la sconfitta, a chi ha cercato di spiegarmi che il terremoto non é solo dovuto al movimento della Terra ma é uno stile di vita, alle lunghe chiacchierate nel tunnel tra l'U1 e l'U2, a chi ha contribuito a scrivere i personalissimi 10 comandamenti del dottorando, a chi é a Berlino ma é come se non fosse mai partita, a chi ha trascorso con me intere giornate di Labex e le notti dei ricercatori, alla mia compagna di camera (e sincera e affidabile confidente) ad Asiago, a chi come me sa emozionarsi ogni volta guardando le oscillazioni di una molla, a chi ha capito che se mi date del cioccolato va tutto bene, a chi ti incontra per i corridoi dell'U2 e non importa che ore siano ma ha sempre un sorriso per te, a chi usa il C solo perché l'ho deciso io, a chi mi dice che devo essere meno indulgente, a chi apprezza le cose fatte proprio "come una Ross",

a chi ha imparato con me che esistono le variabili “mmmm public” e che gli asini mordono, al cioccolato uvetta e rum, alle mie alpine, a chi “manda questa mail, l’hai letta 20184726 volte!!”, a chi é straightforward ma anche un po’ franco e un po’ forte, alle uscite organizzate all’ultimo minuto per rivedere chi torna da Lussemburgo, alla ricerca delle fascette, al sostegno di Brera e infine ad Alfonso... tanti auguri, ma non ti conosco!